

NASA/TP-2010-216128

An errata was added to this document, January 2012



Michigan Orbital DEbris Survey Telescope Observations of the Geosynchronous Orbital Debris Environment

Observing Years: 2002–2003

K. J. Abercromby¹, P. Seitzer², E. S. Barker³, H. M. Cowardin¹, M. J. Matney³, and T. L. Parr-Thumm¹

*¹ESC Group/Jacobs
Houston 77058*

*²University of Michigan
Department of Astronomy
Ann Arbor, Mich. 48109-1042*

*³NASA Johnson Space Center
Houston 77058*

National Aeronautics and
Space Administration

Johnson Space Center
Houston, TX 77058

August 2010

THE NASA STI PROGRAM OFFICE . . . IN PROFILE

Since its founding, NASA has been dedicated to the advancement of aeronautics and space science. The NASA Scientific and Technical Information (STI) Program Office plays a key part in helping NASA maintain this important role.

The NASA STI Program Office is operated by Langley Research Center, the lead center for NASA's scientific and technical information. The NASA STI Program Office provides access to the NASA STI Database, the largest collection of aeronautical and space science STI in the world. The Program Office is also NASA's institutional mechanism for disseminating the results of its research and development activities. These results are published by NASA in the NASA STI Report Series, which includes the following report types:

- **TECHNICAL PUBLICATION.** Reports of completed research or a major significant phase of research that present the results of NASA programs and include extensive data or theoretical analysis. Includes compilations of significant scientific and technical data and information deemed to be of continuing reference value. NASA's counterpart of peer-reviewed formal professional papers but has less stringent limitations on manuscript length and extent of graphic presentations.
- **TECHNICAL MEMORANDUM.** Scientific and technical findings that are preliminary or of specialized interest, eg, quick release reports, working papers, and bibliographies that contain minimal annotation. Does not contain extensive analysis.
- **CONTRACTOR REPORT.** Scientific and technical findings by NASA-sponsored contractors and grantees.
- **CONFERENCE PUBLICATION.** Collected papers from scientific and technical conferences, symposia, seminars, or other meetings sponsored or cosponsored by NASA.
- **SPECIAL PUBLICATION.** Scientific, technical, or historical information from NASA programs, projects, and mission, often concerned with subjects having substantial public interest.
- **TECHNICAL TRANSLATION.** English-language translations of foreign scientific and technical material pertinent to NASA's mission.

Specialized services that complement the STI Program Office's diverse offerings include creating custom thesauri, building customized databases, organizing and publishing research results . . . even providing videos.

For more information about the NASA STI Program Office, see the following:

- Access the NASA STI Program Home Page at <http://www.sti.nasa.gov>
- E-mail your question via the Internet to help@sti.nasa.gov
- Fax your question to the NASA Access Help Desk at (301) 621-0134
- Telephone the NASA Access Help Desk at (301) 621-0390
- Write to:
NASA Access Help Desk
NASA Center for AeroSpace Information
7115 Standard
Hanover, MD 21076-1320



Michigan Orbital DEbris Survey Telescope Observations of the Geosynchronous Orbital Debris Environment

Observing Years: 2002–2003

K. J. Abercromby¹, P. Seitzer², E. S. Barker³, H. M. Cowardin¹, M. J. Matney³, and T. L. Parr-Thumm¹

*¹ESC Group/Jacobs
Houston 77058*

*²University of Michigan
Department of Astronomy
Ann Arbor, Mich. 48109-1042*

*³NASA Johnson Space Center
Houston 77058*

National Aeronautics and
Space Administration

Johnson Space Center
Houston, TX 77058

Errata

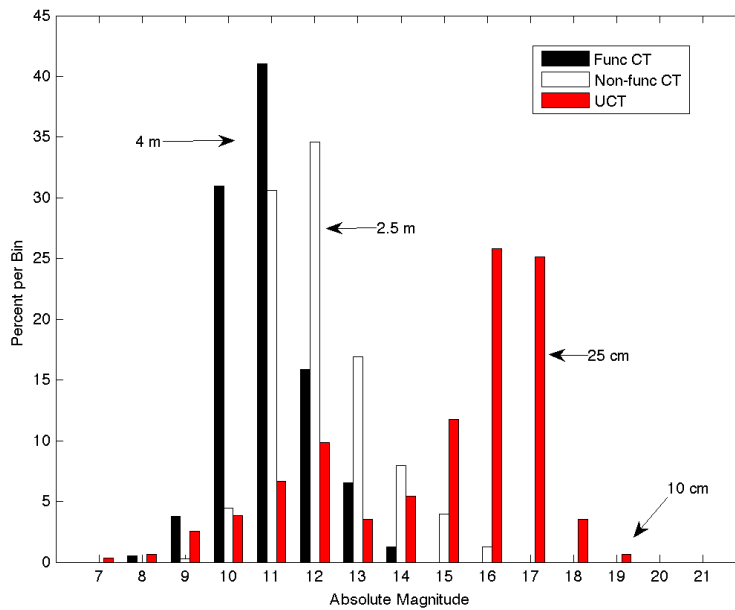
Issued January 2012 for

NASA/TP-2010-216128

Michigan Orbital DEbris Survey Telescope Observations of the Geosynchronous Orbital Debris Environment Observing Years: 2002–2003

K. J. Abercromby, P. Seitzer, E. S. Barker, H. M. Cowardin, M. J. Matney, T. L. Parr-Thumm

Summary of Changes: The figure below replaces figure 1 on pg. 2, and figure 28 on pg. 27.



After publication of the NASA/TP-2010-216128, it was discovered that a few of the fainter correlated targets were labeled as functional targets when they should have been non-functional. The plot above shows the corrected distribution of absolute magnitude versus the percent per bin. The change moved one object from the 15th and one object from the 17th magnitude bin from the functional to non-functional category. This change has no impact on the conclusions drawn in the report nor on any of the other data shown.

Available from:

NASA Center for AeroSpace Information
7115 Standard Drive
Hanover, MD 21076-1320
301-621-0390

National Technical Information Service
5285 Port Royal Road
Springfield, VA 22161
703-605-6000

This report is also available in electronic form at <http://ston.jsc.nasa.gov/collections/TRS/>

Contents

Executive Summary	1
1.0 Introduction.....	3
2.0 Background.....	3
3.0 Observation Overview	3
3.1 The MODEST System	3
3.2 Search Strategy	4
3.3 Data Collection	7
3.4 Data Processing.....	8
3.5 Data Analysis	8
3.5.1 Correlation of detections.....	9
3.5.2 Orbital elements calculation.....	9
3.5.3 Comparison of derived orbital quantities with orbital parameters of known objects	10
3.5.3.1 Inclination	11
3.5.3.2 Mean Motion Determination.....	15
3.5.3.3 RAAN Determination	17
3.6 Summary of Data Processing.....	19
4 Results.....	19
4.1 Detection Rates	19
4.2 Location of Field Centers and Detections.....	19
4.3 Angular Momentum Vector	21
4.4 No-sees.....	24
4.5 Mean Motion Distribution	24
4.6 Inclination Distribution.....	24
4.7 RAAN Distribution	25
4.8 Absolute Magnitude Distribution and Derived Diameters.....	26
4.9 RAAN vs. INC Distribution.....	26
5.0 Conclusions.....	28
6.0 References.....	29
Appendix A: Fields File Example.....	30
Appendix B: Output File Example.....	31
Appendix C: Correlation Output.....	32

Figures

1	Absolute magnitude and derived size distribution assuming an albedo of 0.175 and a diffuse Lambertian phase function	2
2	The MODEST Telescope	4
3	Inclination vs. launch date	5
4	A catalog object showing the date of observation vs. inclination. These data show the progression of INC over time, with the noise being bad data points	5
5	RAAN vs. INC for near-GEO objects for a given date	6
6	Daily motion for GEO objects (RA vs. DEC) as viewed from CTIO, Chile.....	7
7	Sample mosaic of nine frames of MODEST data. The object (seen as a point) appears in the middle of the left-hand side of the figure and traverses to the upper right corner. This image is the width (RA) of the FOV but only one-fourth of the height (DEC). The streaks in this image are stars	8
8	Geometry for computing orbital parameters.....	11
9	INC comparison for correlated targets separated into functional (F) and nonfunctional (NF) categories. CY 2002 is on the left and CY 2003 is on the right.....	12
10	INC comparison for correlated targets separated into functional (F) and nonfunctional (NF) categories, concise range. CY 2002 is on the left and CY 2003 is on the right.....	13
11	INC error as a function of INC, entire range	14
12	INC error as a function of INC, concise range	14
13	Comparison of inferred and known mean motion	15
14	Comparison of inferred and known mean motion, concise range	16
15	Mean motion error vs. ACO mean motion	16
16	Comparison of inferred and known RAAN.....	17
17	RAAN error as a function of INC.....	18
18	RAAN error (focus on smaller errors) as a function of INC	18
19	Location of field centers	20
20	Probability of finding specific orbits based on field center locations.....	20
21	Angular momentum vector of an orbit	21
22	Polar coordinates for objects, CY 2002	22
23	Polar coordinates for objects, CY 2003	23
24	Polar coordinates with probability and detections overlaid.....	23
25	Mean motion distribution for CT and UCT objects.....	25
26	Distribution of INCs for CTs and UCTs.....	25
27	Distribution of RAAN for CTs and UCTs. The location of the data found is biased by the field center selection and the DOY.....	26
28	Absolute magnitude and derived size distribution, assuming an albedo of 0.175 and a diffuse Lambertian phase function.....	27
29	RAAN vs. INC for CT and UCT objects.....	27

Tables

1	Inclination Errors for CY 2002 and CY 2003.....	12
2	Mean Motion Errors	15
3	RAAN Errors.....	17
4	Statistics on CY 2002 and CY 2003 Data Collection.....	19

Acronyms

ACO	assumed circular orbit
CCD	Charge-Coupled Device
CDT	CCD Debris Telescope
CIS	Commonwealth of Independent States
CT	correlated target
CTIO	Cerro Tololo Inter-American Observatory
CY	calendar year
DEC	declination
DOY	day of year
F	functional [only used in figure callouts]
FOV	field of view
FWHM	full width at half maximum
GEO	geosynchronous orbit
GEODSS	Ground-based Electro-Optical Deep Space Surveillance
HA	hour angle
INC	inclination
JSC	Johnson Space Center
LST	local sidereal time
MODEST	Michigan Orbital DEbris Survey Telescope
NF	nonfunctional [only used in figure callouts]
OH	oxygen-hydrogen-bond emission
RA	right ascension
RAAN	right ascension of ascending node
RMS	root mean square
S/N	signal to noise
SGP	Simplified General Perturbation code
SSN	Space Surveillance Network
TDI	time delay integration
TLE	two-line element
UCT	uncorrelated target
UT	universal time

Executive Summary

NASA uses the Michigan Orbital DEbris Survey Telescope (MODEST), the University of Michigan's 0.61-m aperture Curtis-Schmidt telescope at the Cerro Tololo Inter-American Observatory in Chile, to help characterize the debris environment in geosynchronous orbit; this usage began in February 2001 and continues to the present day. Detected objects that are found to be on the U.S. Space Surveillance Network cataloged objects list are termed correlated targets (CTs), while those not found on the list are called uncorrelated targets (UCTs).

This Johnson Space Center report provides details of observational and data-reduction processes for the entire MODEST dataset acquired in calendar years (CYs) 2002 and 2003. Specifically, this report describes the collection and analysis of 35 nights of data collected in CY 2002 and 16 nights collected in CY 2003.

MODEST is equipped with a 2.048×2.048-pixel charged coupled device camera with a 1.3 by 1.3 deg field of view. This system is capable of detecting 19th-magnitude objects using a 5-s integration that corresponds to a 10-cm diameter, 0.175-albedo object at 36,000 km altitude, assuming a diffuse Lambertian phase function. For both years, averages of 23 objects were detected each night. On average in CY 2002, 76% of the detections were CTs and 24% were UCTs, whereas in CY 2003 the percentages were 66% and 34% for CTs and UCTs, respectively. The differences may be due to observing in different locations.

From the correlated objects, estimates can be made as to the errors associated with the derived quantities of range, inclination (INC), and right ascension of ascending node (RAAN) compared to quantities determined using an assumed circular orbit. The average INC root mean square (RMS) error is 0.1° for functional CTs and 0.3° for nonfunctional CTs. Since RAAN is ill-defined at small values of INC (those less than 1°), the RMS error for RAAN is calculated for only objects with INC greater than 1°. The average RAAN RMS error is 20° for functional objects and 11° for nonfunctional objects in CY 2002, and 57° for functional objects and 16° for nonfunctional objects in CY 2003. For CY 2002, the mean motion error is 0.0005 for functional and 0.0070 for nonfunctional objects and 0.0071 and 0.0091 for functional CTs and nonfunctional CTs, respectively. This error analysis of CT values for INC, RAAN, and mean motion lends credibility to the determination of the UCT orbital distributions.

Figure 1 shows the size distribution of 1,137 objects detected in the data processed for CY 2002 and CY 2003. The actual peak of the absolute magnitude distribution for the functional correlated targets is 11th magnitude. An absolute magnitude of 11.5 corresponds to objects having average diameters of 4.6 m, assuming an albedo of 0.175 and a diffuse Lambertian phase function. This result generally agrees with the known sizes of intact satellites. The absolute magnitude distribution for the UCTs is broad but starts to roll off near a diameter of 29 cm or 17.5 magnitude. The roll off in distribution reflects the detection capability of MODEST, and not the true nature of the population. The true population is believed to continue at the same slope through fainter magnitudes.

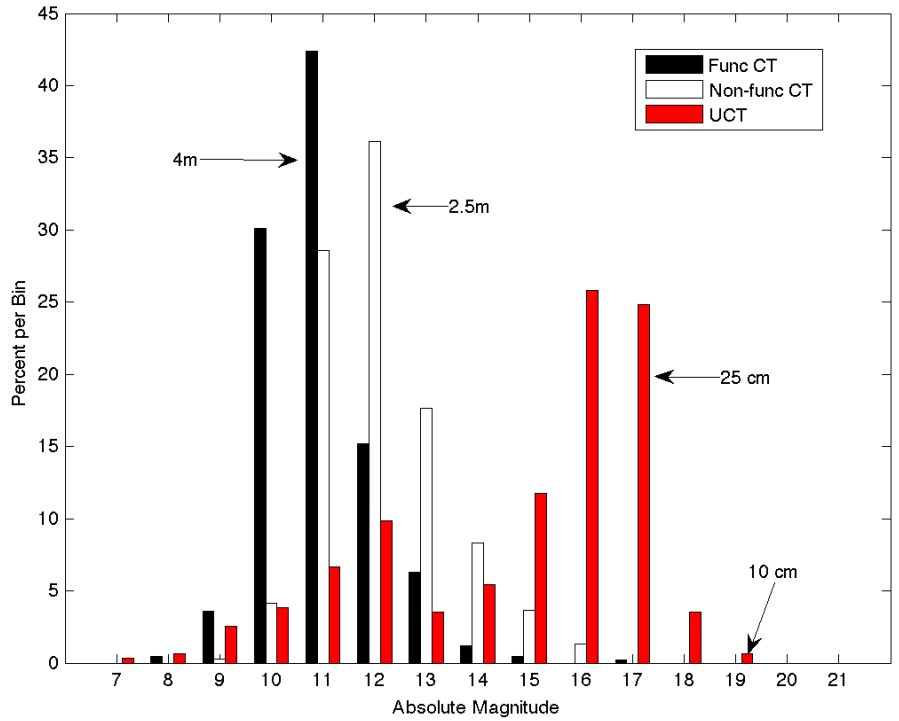


Figure 1. Absolute magnitude and derived size distribution assuming an albedo of 0.175 and a diffuse Lambertian phase function.

1.0 Introduction

Orbital debris is a concern to all nations that use satellites or launch space vehicles. The debris field scattered near Earth's geosynchronous orbit (GEO) poses a threat to anything residing in or passing through it. To mitigate risk and minimize this environment's expansion, the environment must be understood. NASA uses the Michigan Orbital DEbris Survey Telescope (MODEST), a University of Michigan-owned 0.61-m aperture Schmidt telescope at Cerro Tololo Inter-American Observatory (CTIO) in Chile, to help characterize the debris environment in GEO. The objectives for this survey are to determine the extent and character of debris in GEO, specifically by obtaining distributions for the brightness, inclination (INC), right ascension of ascending node (RAAN), and mean motion for the debris.

2.0 Background

The GEO environment's debris population has a high potential for collision with operational satellites due to the extremely long lifetimes of debris and satellites. Space-faring nations have been placing satellites into GEO since the mid- to late-1960s. Along with operational satellites, debris consisting of dead satellites, rocket body upper stages, deployment hardware, small debris, etc., has been placed into GEO. To date, two breakups have been reported in GEO. The first of these, the 1978 breakup of an EKRAAN 2 satellite, Space Surveillance Network (SSN) 10365, went unreported prior to its identification in 1992 by the Commonwealth of Independent States (CIS).¹ In 1992, a Titan 3C Transtage breakup,^{1,2} SSN 3432, produced at least 20 pieces. The Ground-based Electro-Optical Deep Space Surveillance (GEODSS) telescopes tracked these objects for a few days after the event, but all but eight pieces have been lost.

NASA used the Charged-Coupled Device (CCD) Debris Telescope (CDT), a transportable 32-cm Schmidt telescope, to conduct initial GEO surveys. The CDT was shipped to the Hawaiian island of Maui for a survey of the GEO environment conducted by NASA from 1992 through 1994.³ Results from this survey indicated that, to a limiting apparent magnitudes of 17 (~60 cm in diameter), about 27% of all objects in GEO are debris. The actual debris population will be much larger due to the presence of objects smaller than 60 cm in diameter. NASA moved the CDT to Cloudcroft, NM, for further GEO studies, where data were collected from November 1997 to December 2001. Due to funding issues, the CDT was shut down in December 2001.

The MODEST program benefited from the data collected by the CDT as the CDT determined the rate at which most GEO objects are traveling.

3.0 Observation Overview

3.1 The MODEST System

The MODEST system uses the University of Michigan's Curtis-Schmidt telescope located at the CTIO in Chile. Since February 2001, the telescope has been dedicated to optical studies of orbital debris for NASA's Orbital Debris Program Office at the Johnson Space Center (JSC).

The telescope is a 0.61-m aperture, f/3.5 Schmidt of classical design, with a CCD mounted at a Newtonian focus. The CCD is a thinned, backside-illuminated device manufactured by SITE. The format is 2,048 × 2,048 pixels, each of which is 24 microns square. This provides a sampling of 2.318 arc-seconds/pixel, and a 1.3×1.3-deg field of view (FOV).

A 5-s exposure through a broad R filter centered at 630 nm and 200 nm wide (full width at half maximum [FWHM]) produces a signal-to-noise (S/N) that is equal to 10 on a point source detection of 18th R magnitude under typical dark sky conditions at CTIO.

A picture of the MODEST telescope is shown in Figure 2.



Figure 2. The MODEST telescope.

3.2 Search Strategy

Numerous studies^{4,5} provide compelling arguments that most uncontrolled debris objects in GEO should be at INCs that are less than or equal to 15°. Orbits of uncontrolled GEO objects oscillate around the stable Laplacian plane, which has an INC of 7.5° with respect to the equatorial plane. This oscillation is dominated by the combined effects of the Earth's oblateness (J2 term) and solar and lunar perturbations. The INC oscillation period is about 50 years. During the first 25 years, an uncontrolled object with an initial INC of 0° will gradually increase in INC until its INC has peaked at 15°. During the next 25 years, this same object's INC will gradually decrease until it has returned to its original INC, in this case, 0°, and it will begin its oscillation cycle again. Most uncontrolled objects with a different initial INC will follow the same 50-year pattern of increasing their INC to 15°, decreasing to 0°, and then returning to their original INC. (There are some cases in which the INC will first decrease to 0°.) Depending on the insertion RAAN, an uncontrolled object's oscillation can be out of phase with other objects, although these examples are few.

Figure 3 shows the INC of objects in GEO plotted against their launch date. These data were taken from the element set file as of day 365, year 2003, and plots 2,884 objects. All objects plotted have mean motions of less than 1.1 revs/day. The oldest have already peaked in INC and are now approaching 0° INC again. Figure 4 shows one catalog object's progression in INC over time. This object's INC increased to 15° and is on its way toward decreasing back to 0°. There is also a strong correlation between an object's INC and its RAAN, as illustrated in Figure 5.

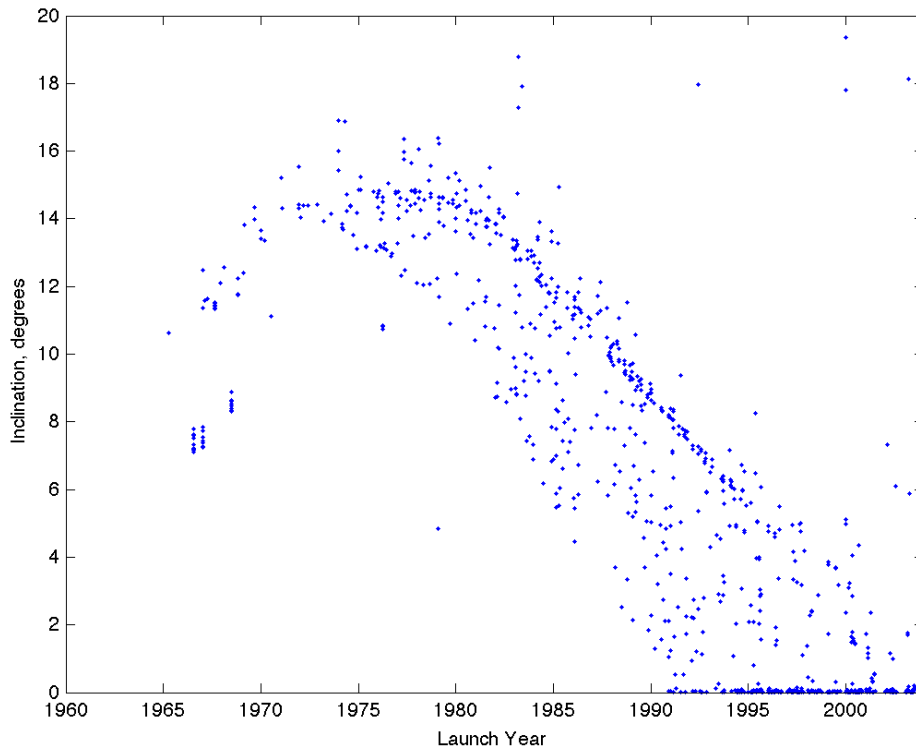


Figure 3. Inclination vs. launch date.

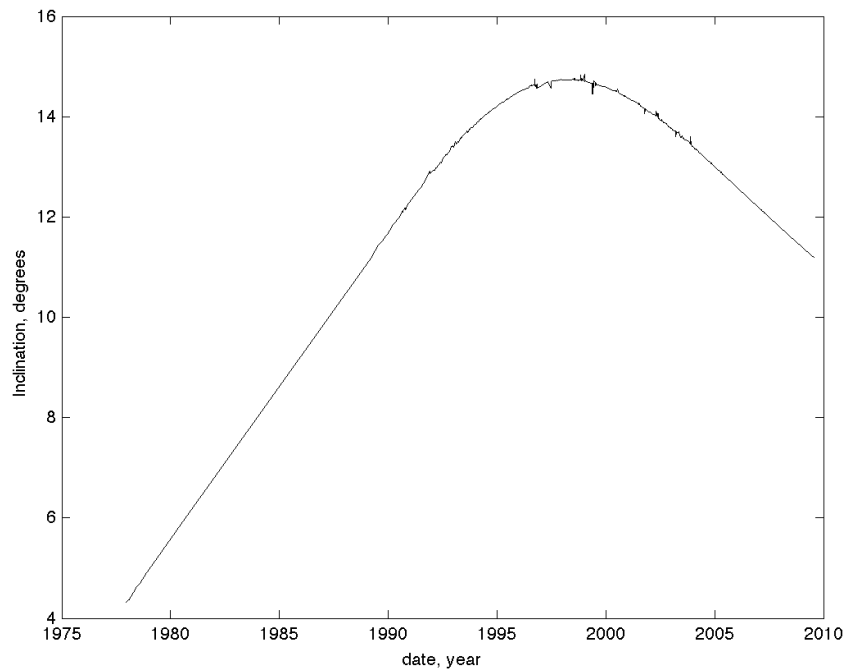


Figure 4. A catalog object showing the date of observation vs. inclination. These data show the progression of INC over time, with the noise being bad data points.

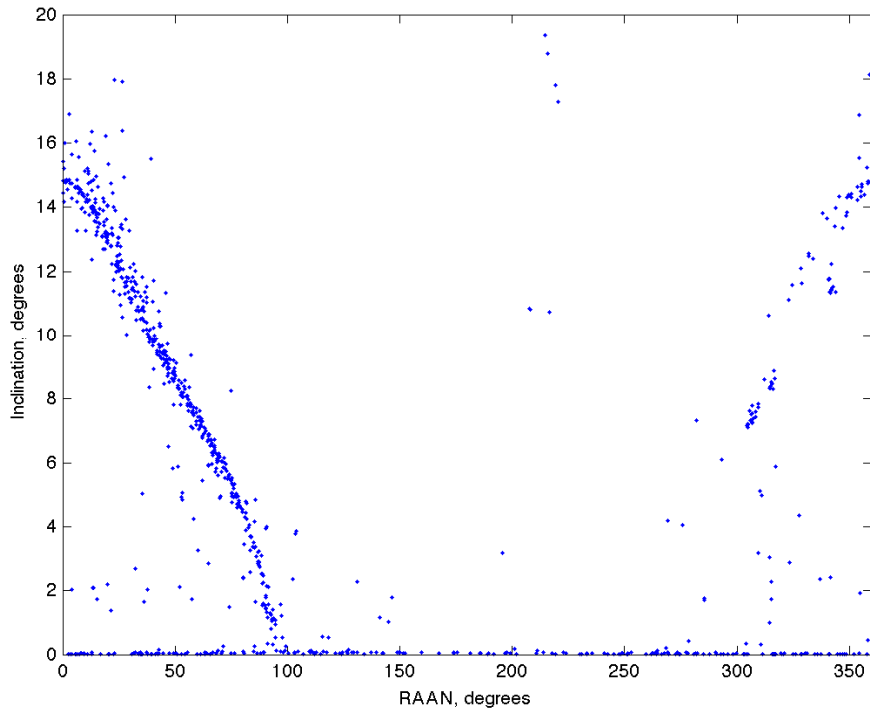


Figure 5. RAAN vs. INC for near-GEO objects for a given date.

Figure 6 illustrates the daily motion for a set of objects having mean motions less than 1.1 revs/day and INCs less than 17° . These data are for a given date and time in 2003. Since most orbital debris will be associated with operational satellites, searches need to be made above or below the equator at the appropriate times to maximize the detection rate of the debris. While there may be a few very interesting objects outside this envelope, most debris will be found near or inside the envelope. As a result of the systematic orientation of the orbital planes, objects with a given INC will be above (or below) the Earth's equator at the same time.

To date, the best way found to represent orbital debris magnitude variations as a function of phase angle is a Lambertian phase function, in which the maximum brightness is observed at the 0° phase angle.⁶ To detect the smallest debris possible, it is best to observe the debris under nearly face-on (small phase angle) solar illumination. This condition is most closely reached for objects near the anti-solar point. Since Earth's shadow projected into space has a finite angular diameter, on the order of 17° at geosynchronous distances, it is impossible to meet the condition of exact face-on illumination (phase angle = 0°).

From MODEST's location, orbital longitudes can be seen from 25°W to 135°W . Each night, MODEST observers determine a specific right ascension (RA) and a declination (DEC) that is the closest to the anti-solar point as possible without being in the Earth's shadow. The telescope then stares at that location for the night. However, on nights near the equinoxes when Earth's shadow overlaps the region of interest, two fields are observed by switching locations halfway through the night, with the first half of the night leading the shadow of the Earth and the second half of the night trailing the shadow. All telescope-pointing locations are determined prior to the start of the run. The location of the moon also plays a role as to when observations can occur. As a general rule, observations take place ± 1 week around the new moon.

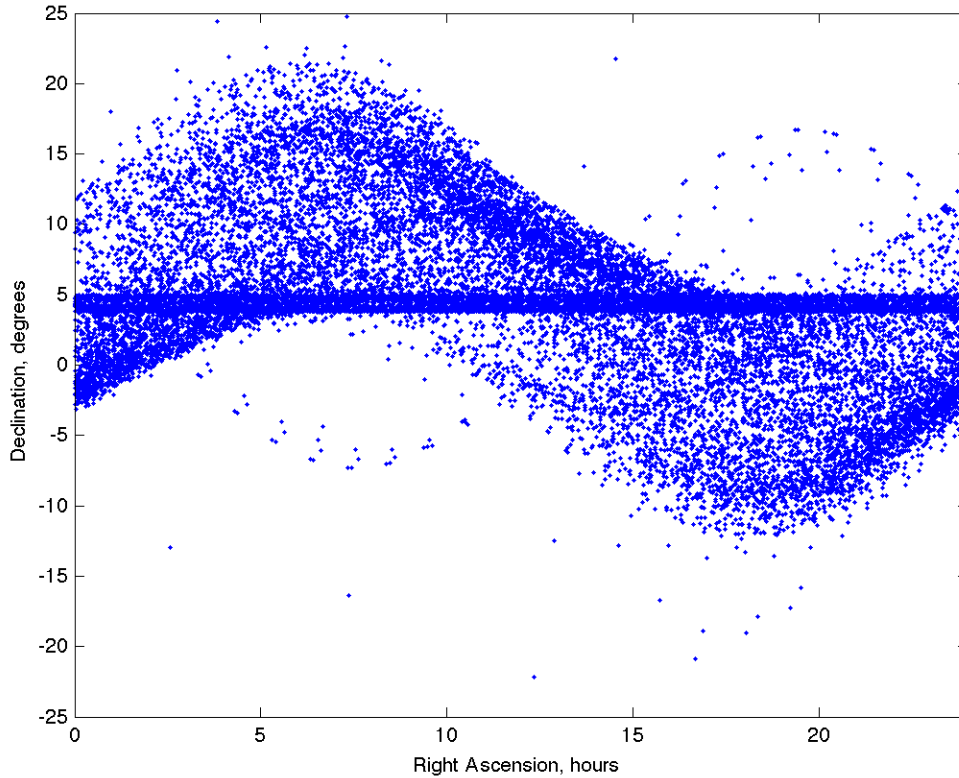


Figure 6. Daily motion for GEO objects (RA vs. DEC) as viewed from CTIO, Chile.

3.3 Data Collection

The telescope tracks at the sidereal rate in RA and a fixed DEC. The CCD chip is aligned on the telescope such that the RA vector is parallel to the shift registers. During the 5-s exposure, the charge on the CCD is shifted in reverse so that objects are seen as a point source and stars are seen as streaks. This mode is known as time delay integration (TDI). Thus, the system has peak sensitivity to objects with the expected motion of GEO objects. Objects orbiting the Earth can appear as streaks depending on their altitude and INC.

The standard exposure time is 5-s with a total time between exposures of 37.9 s. An S/N of 10 corresponds to about an 18th-magnitude limit for one detection. The frame number, RA, DEC, instrumental magnitude, epoch, observation date, and universal time (UT) are calculated for each detection of each object. Instrumental magnitude is transformed to an R magnitude by observing standard Landolt stars. A broad R filter centered at 630 nm and with FWHM = 200 nm is used for observing. This passband maximizes the final S/N of faint objects by minimizing the signal from the night sky. It also minimizes the scattering of moonlight below 400 nm and OH emissions above 800 nm. Four independent detections are required to consider that a possible target is a real object. At the first detection, a computer program (debris finder) determines where the next detection should be for the object given a rate box movement of ± 2 arc-second/second in hour angle (HA) and ± 5 arc-second/second in DEC. For GEO objects, the total time spent in the FOV is generally 5 min. Figure 7 shows a mosaic of nine frames in a MODEST data set. The object can be seen traveling from the middle left to the upper right as time increases.

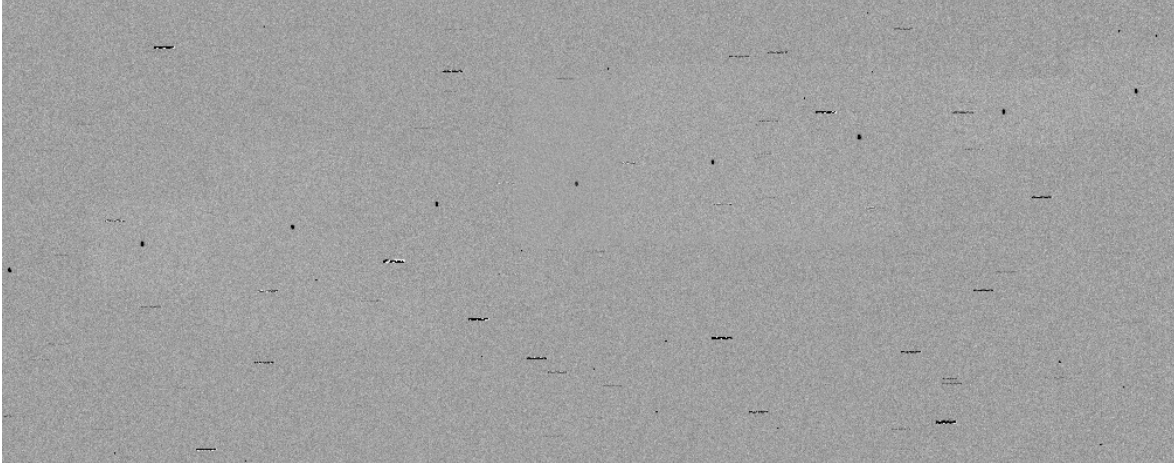


Figure 7. Sample mosaic of nine frames of MODEST data. The object (seen as a point) appears in the middle of the left-hand side of the figure and traverses to the upper right corner. This image is the width (RA) of the FOV but only one-fourth of the height (DEC). The streaks in this image are stars.

In addition to computer detection of objects, a manual review of one night is conducted every 4 months. The manual review consists of two people observing the frames collected in a given night and recording the frames in which objects are seen. These manual observations are then compared to the computer detections to make sure the computer code is catching all the objects it should. In all manual reviews to date, the computer has found 100% of the objects it should, so extreme confidence is established in the ability to find objects that fall within the rate box.

3.4 Data Processing

A real-time data-reduction pipeline has been implemented at MODEST that performs the following steps:

- Removes the instrumental signature on each image. This involves subtracting the bias over-scan from each amplifier section, subtracting a master bias to remove low-level bias structure, and dividing by a normalized flat field to remove pixel-to-pixel sensitivity variations.
- Finds potential debris candidates that are either point sources or short streaks (<10 pixels long). This debris finder is insensitive to the 32-pixel-long star streaks.

At the end of the night, a frame-to-frame correlator is run on the candidate lists from all survey images. The output of this correlator is a list of all potential debris candidates that appear in four or more frames, together with their positions and magnitudes. It is assumed that real objects move linearly through subsequent frames.

A nightly manual review of all candidates that have five or less detections is performed at the telescope. False positives (largely due to cosmic rays and the end of star streaks) are rejected by the operator. Experience demonstrates that there are no false positives with six or more detections.

3.5 Data Analysis

This section describes the process of converting the lists of observations (date, UT, RA, DEC, and magnitude) from the position files into lists of cataloged objects, both correlated targets (CTs) and uncorrelated targets (UCTs), as well as their derivable orbital parameters.

3.5.1 Correlation of detections

Once the data are received by JSC, the correlation of detections is conducted. For each exposure, the day, year, UT, and the field center of the FOV are determined. Then, using an augmented version of the Simplified General Perturbation code (SGP), the satellite catalog is compared to the RA, DEC, and time of each exposure to determine whether an object might be in the FOV. An attempt is carried out to correlate all satellites within a 1° radius of the center of the FOV with any detected object. The results are then output to a file containing all information for all exposures within a given night. Appendix C lists a subset of that file. The program is written with a larger FOV than the true one so that, if any pointing errors arise, a possible correlation still can be obtained.

To correlate an object that was predicted to be in the FOV with one found in a specific frame, a missed distance is calculated. Missed distance is defined as the absolute value of the squared difference between the observed and the predicted RA and DEC positions. A nightly offset, calculated by taking the average value of the missed distance, is then subtracted from the missed distance. Epoch dates (age of an element set) are known to impact the accuracy of where an object is predicted vs. where it is actually located on a given night. This missed distance is not expected to change dramatically as the accuracy of the catalog from year-to-year stays consistent.

If the missed distance is within 0.025° , the software counts the object as a CT. If an object in the FOV cannot be correlated to an object in the catalog, that object is labeled as a UCT. If an object is predicted to be in the FOV but is not seen, it is termed a “no-see.” Each correlation is inspected by hand and an override of a computer correlation or non-correlation is possible. On average, 10% of the correlations are done by hand while the computer correlates the remaining 90% of the objects. Most of the hand correlations are done when there are multiple objects, both observed and predicted, in the FOV at the same time.

3.5.2 Orbital elements calculation

The orbit fit program uses a multidimensional simplex optimization routine to fit an orbit to the observations.⁷ The observations consist of a series of time-tagged RA and DEC points. The optimization routine finds an orbit that, when propagated to a state vector at the times of individual observations, would appear in the correct positions as viewed from the telescope (with Earth rotation and telescope location included). The parameter to be optimized is the angular distance (averaged over the number of unique observations) between the predicted and the computed positions.

Standard Kepler orbital elements tend to be very poor-fitting parameters, especially for orbits with near-zero inclinations and low eccentricities (eg, GEO orbits) in which elements such as an ascending node and an argument of perigee become ill-defined. However, an ideal one-to-one conversion exists between any ideal Kepler orbit and a state vector (both referenced to the same epoch). State vectors are attractive candidates for fitting an orbit because they can be varied smoothly without any ill-defined points, at least over a wide range of possible values.

However, using an ideal Kepler orbit may be inadequate for actual orbit fitting. It would also be useful to include at least the most basic of perturbing terms for realistic orbit predictions. This is accomplished by using the SGP propagator,⁸ which includes estimates of the effects of the J_2 term in the Earth's geopotential. The input for SGP is a two-line element (TLE) set that has the same form as classical Kepler orbital elements.

The fitting procedure varies the pseudo-state-vector parameters (defined at a reference epoch for that observation), which are converted directly to Keplerian orbital elements. This Kepler orbit is then treated as the elements of a TLE appropriate for the SGP subroutine. SGP then delivers position predictions at each of the observation times for that orbit, and these positions are compared to the positions that are ac-

tually measured until a best-fit solution is achieved. Only the TLE orbit is then recorded that produced the optimized fit.

In general, short-arc data are of insufficient quality to compute an accurate orbit eccentricity. However, by penalizing any eccentricity above zero in the optimization portion of the code, a circular-orbit solution can be found.

3.5.3 Comparison of derived orbital quantities with orbital parameters of known objects

The accuracy of the orbital parameters, mean motion, INC, and RAAN for debris can be inferred from the observations of CTs. The error seen in the orbital parameter is due largely to the departures from the circular orbit approximation used in calculating the orbital element. In this report, assumed circular orbit (ACO) is the term that describes the orbital element derived from the assumption of a circular orbit. In a similar fashion, the terms “known elements” or “SATRAK [Satellite Tracking (Government-owned propagator)] elements” are used interchangeably for elements obtained from cataloged TLE sets. In this report, the terms “inferred” and “known” are used most of the time when discussing data stemming from SATRAK or TLEs.

The viewing geometry for computing the orbit of an object that passes through the FOV is illustrated in Figure 8. The rectangular geocentric equatorial coordinate system is used. The X-axis points in the direction of the vernal equinox, the Y-axis lies in the plane of the equator and points towards longitude 90°, and the Z-axis points towards the celestial north pole. Both the orbital INC, i , and the RAAN can be calculated using the spherical triangles in Figure 8. From the spherical triangle defined by points A – the RAAN; B – the sub-Earth satellite position; and P – the Earth’s pole,

$$i = \cos^{-1}[\sin(CBA)\cos(BC)]$$

$$\Delta\lambda = \sin^{-1}[\tan(BC)/\tan(i)]$$

$$RAAN = LST + \Delta\lambda$$

where CBA is the angle at which the object crosses the FOV, BC is the sub-satellite latitude, $\Delta\lambda$ (angle CA) is the longitude difference between the sub-satellite longitude and the orbit’s ascending node, and LST is the local sidereal time. The proper quadrant for the longitude difference can be determined by inspection. A reasonable estimate of an observed debris object’s altitude can be obtained from the distance it moves along the arc AB during the exposure sequence and by assuming it is in a circular orbit. By knowing the altitude, the mean motion can be determined.

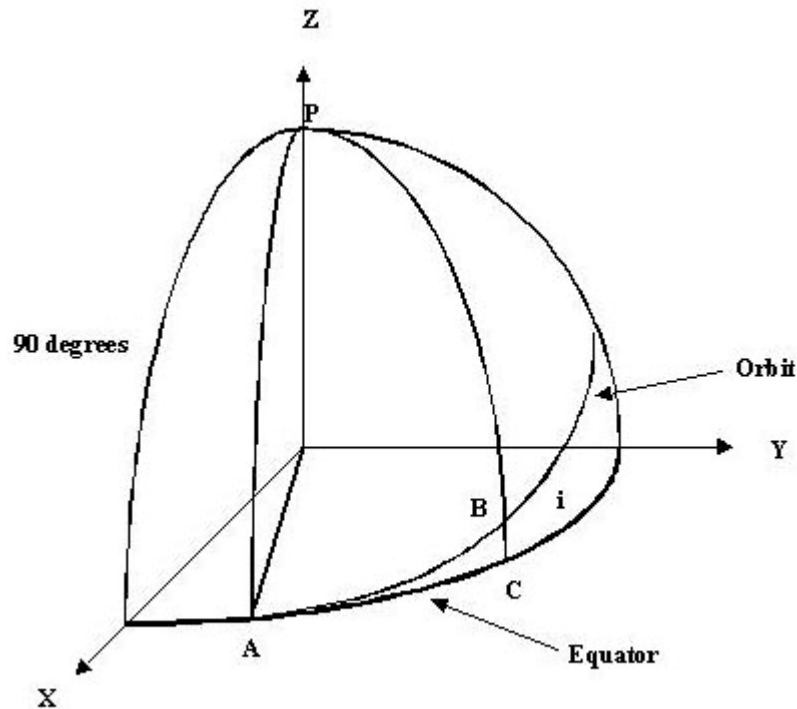


Figure 8. Geometry for computing orbital parameters.

Errors associated with determining the orbital parameters are dependent on the time span over which the observations were obtained, the INC of the orbit, the eccentricity of the orbit, and the actual pixel size of the CCD.

The root mean square (RMS) of the error is calculated for most of the elements using the calculated element and the TLE element for the CT objects. In addition, for some elements the category of CT is further broken into functional and nonfunctional objects. The distinction is whether or not the object is believed to be station-kept. Station-kept is defined as those objects that are allowed to drift in the north-south direction but not in the east-west direction. If an object is station-kept, it is termed a functional CT; if not, it is termed a nonfunctional object. There are two reasons for this distinction. First, it is believed that nonfunctional objects should show similar characteristics to orbital debris, thus giving a better estimate of the imposed error on the determination of the orbit. Second, it is possible that a maneuver occurred with a functional object after the TLE was published and before the observation of the object. If this is the case, the TLE and the calculated element would show differences that are not errors in the process of calculating the orbit but rather, show that the object is no longer in the same orbit. However rare this case may be, it should be considered.

3.5.3.1 Inclination

The inclination of the orbit is the least error-prone of the elements calculated for most objects. The RMS error for INC is shown in Table 1. The errors are similar for both calendar years (CYs), meaning that regardless of the locations observed, the errors are consistent. The data in the table also break down the errors for functional and nonfunctional objects. Functional objects are those believed to be actively station-keeping, whereas nonfunctional objects appear not to be station-kept.

Table 1. Inclination Errors for CY 2002 and CY 2003

Types of Error (reported in degrees)	Functional Objects	Nonfunctional Objects
RMS 2002	0.1	0.3
RMS 2003	0.2	0.1

Figure 9 shows the ACO INC vs. predicted INC for functional and nonfunctional targets. The solid line indicates where the quantities are equal. Both years show good agreement, and this was an expected result. There are some outliers on the 2002 data above a predicted INC of 10° and one outlier near 6°. These objects were investigated and were found to have eccentricities larger than 0.4. With the circular orbit assumption, it is understandable that the INC would be off, even slightly, for these objects.

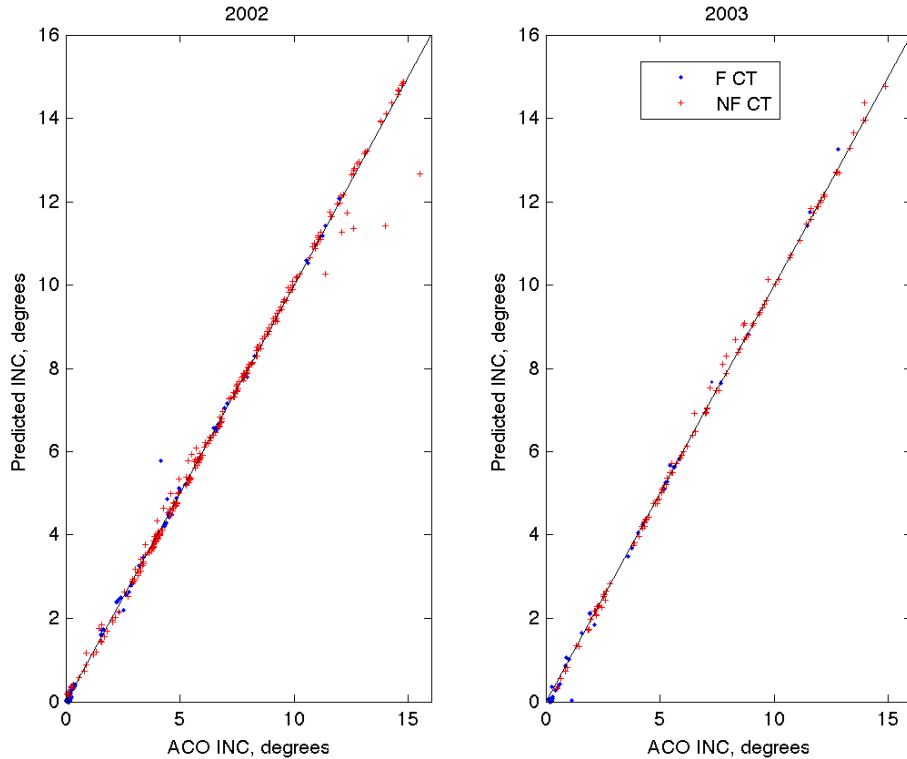


Figure 9. INC comparison for correlated targets separated into functional (F) and nonfunctional (NF) categories. CY 2002 is on the left and CY 2003 is on the right.

In Figure 10, the same data are used; however, the scale is much smaller so the region less than 1° can be investigated. As seen in the figure, the ACO INC is overestimating the INC as referenced to the TLEs in all cases for both years. Measures currently are being taken to correct this offset, including correcting any possible pointing errors from the telescope. However, the error is still very small and may not be significant compared to other sources of error.

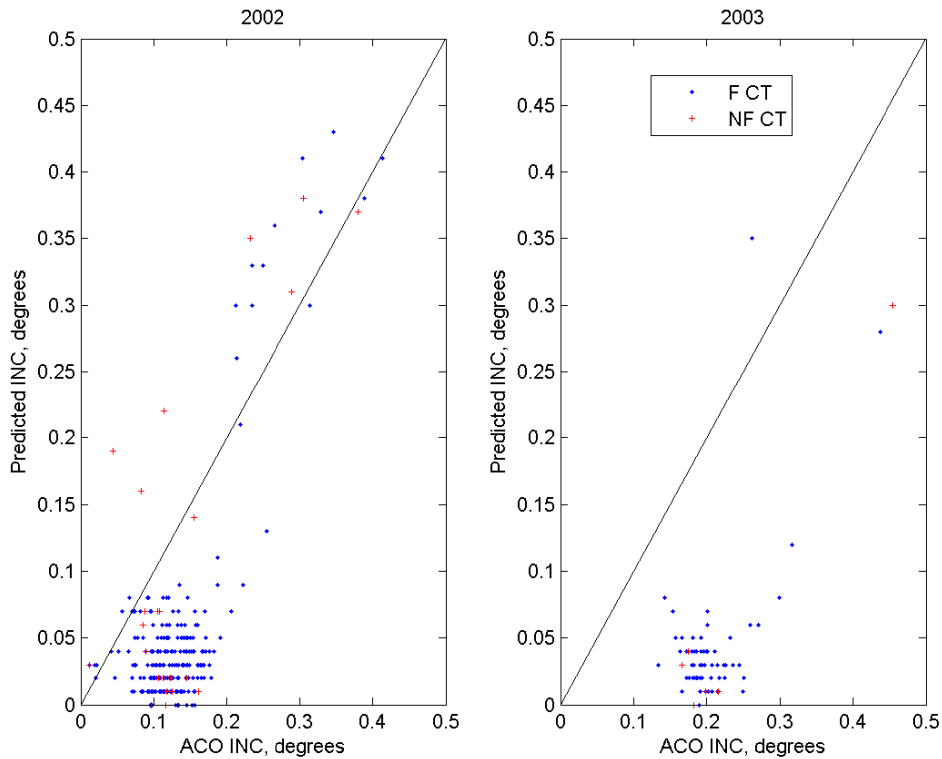


Figure 10. INC comparison for correlated targets separated into functional (F) and nonfunctional (NF) categories, concise range. CY 2002 is on the left and CY 2003 is on the right.

An examination of the error in INC vs. the ACO INC was investigated, and the results are shown in Figure 11 and Figure 12 for both the entire range and a more concise range of inclinations, respectively. From this point forward, the more concise range is used when the X- or Y-axis is changed to show greater detail in one part of the figure. This examination was conducted to determine whether large errors were seen at any specific INC or within functional or nonfunctional objects. The 2002 data showed what was expected from previous charts. The functional objects gather near 0° and have errors showing underestimation of the INC. The nonfunctional objects have an equal spread between over- and underestimation of the INC throughout all INC ranges. However, the 2003 data were slightly different. The functional objects behaved as one would expect, but the nonfunctional data were almost all underdetermined. A cause for this was examined but no correlation could be found near the observational area, the objects themselves, or the way inclination is calculated. Investigations are still underway.

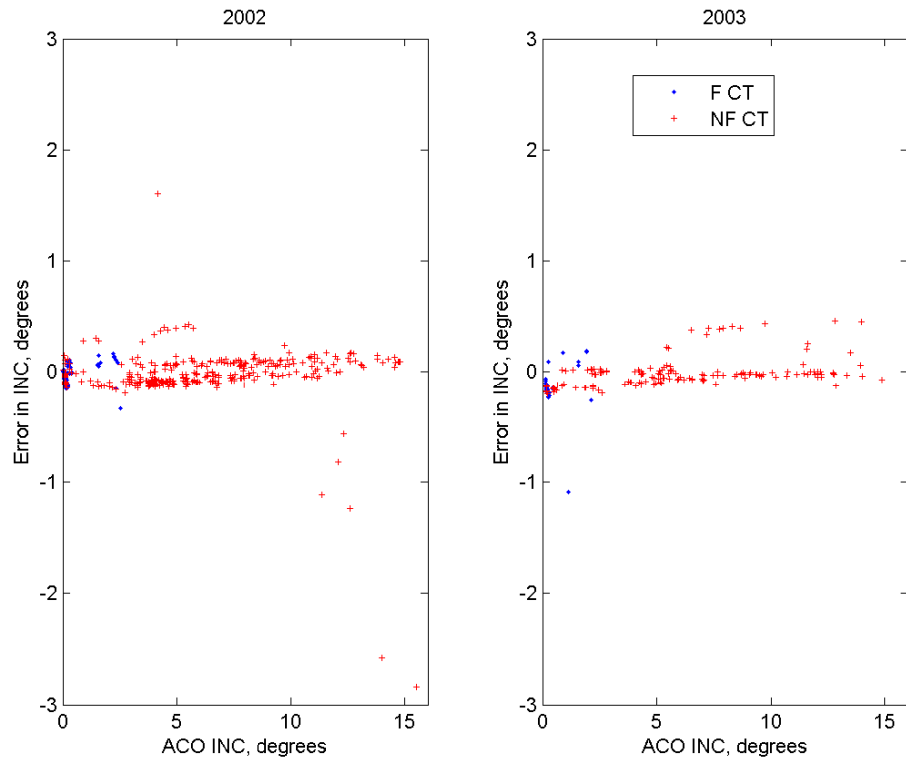


Figure 11. INC error as a function of INC, entire range.

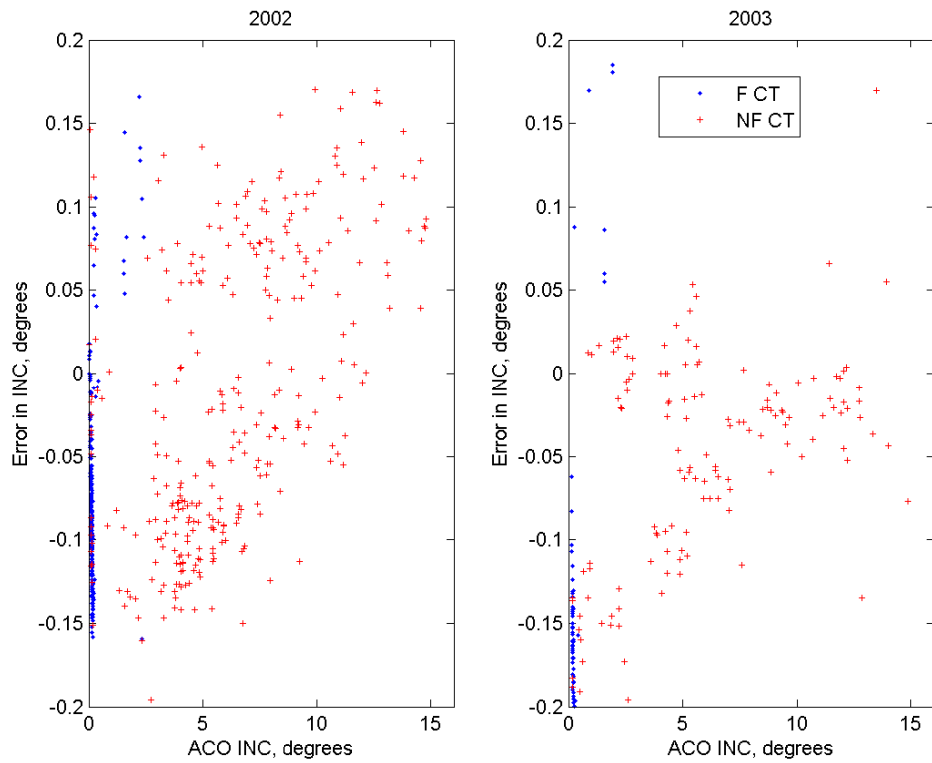


Figure 12. INC error as a function of INC, concise range.

3.5.3.2 Mean Motion Determination

The usual mean motion for geostationary objects is near 1.0027 revs/day. The RMS error for mean motion is shown in Table 2. The errors are very small for both years, meaning that regardless of the locations observed, the errors are consistent. The errors for nonfunctional objects are slightly larger than those for functional objects; but again, the errors for both cases are very small.

Types of Error	Functional Objects	Nonfunctional Objects
RMS 2002	0.0005	0.0070
RMS 2003	0.0071	0.0091

The data for mean motion are plotted in a similar fashion to that seen in the section for inclination. A comparison of the ACO mean motion vs. the predicted (TLE) mean motion is shown in Figure 13, and a more concise range of mean motions using the same data is shown in Figure 14. The data shown in Figure 13 center around the mean motion of 1, which is to be expected. Some of the data fall above and below these data, meaning that the data were collected on both sub-synchronous and super-synchronous GEO objects. Figure 14, where the data are shown in a more concise range of values, shows a straight line through a predicted value of 1.0027 revs/day, but that value has a range of possible values for the ACO mean motion. No reason can be found to explain the results. Although this looks like a large error, by examining the range in values it is seen that this error is very small.

The data in Figure 15 show the error in mean motion vs. the ACO mean motion. The spread in the error is spaced equally between negative and positive values in error. However, there is a slight slope from the upper left to the lower right. No reason for this slope could be obtained.

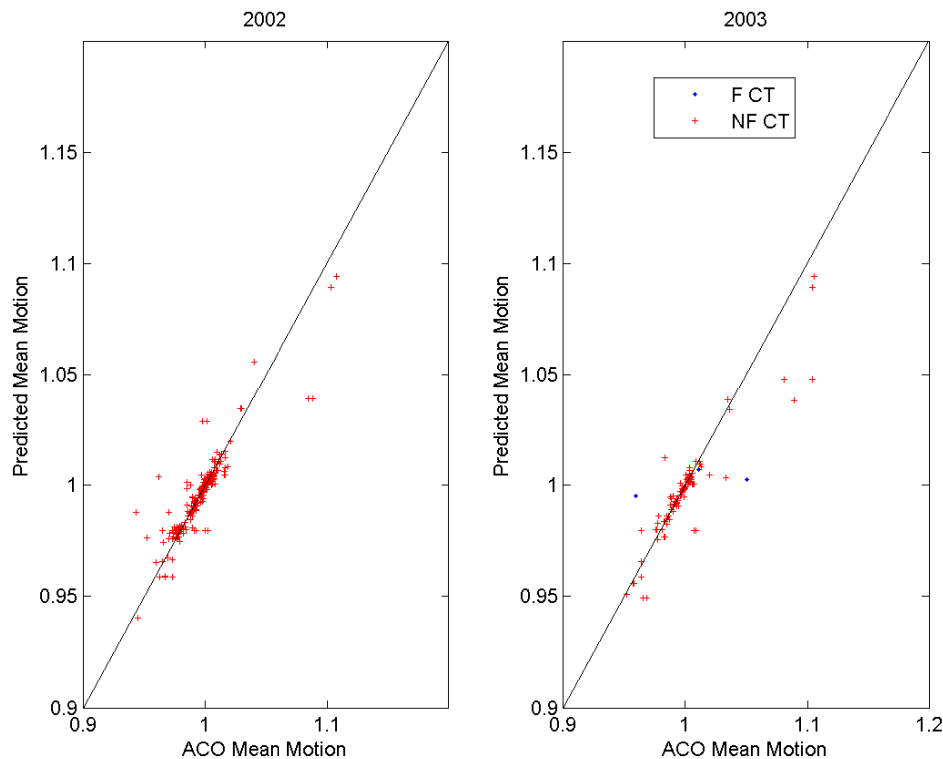


Figure 13. Comparison of inferred and known mean motion.

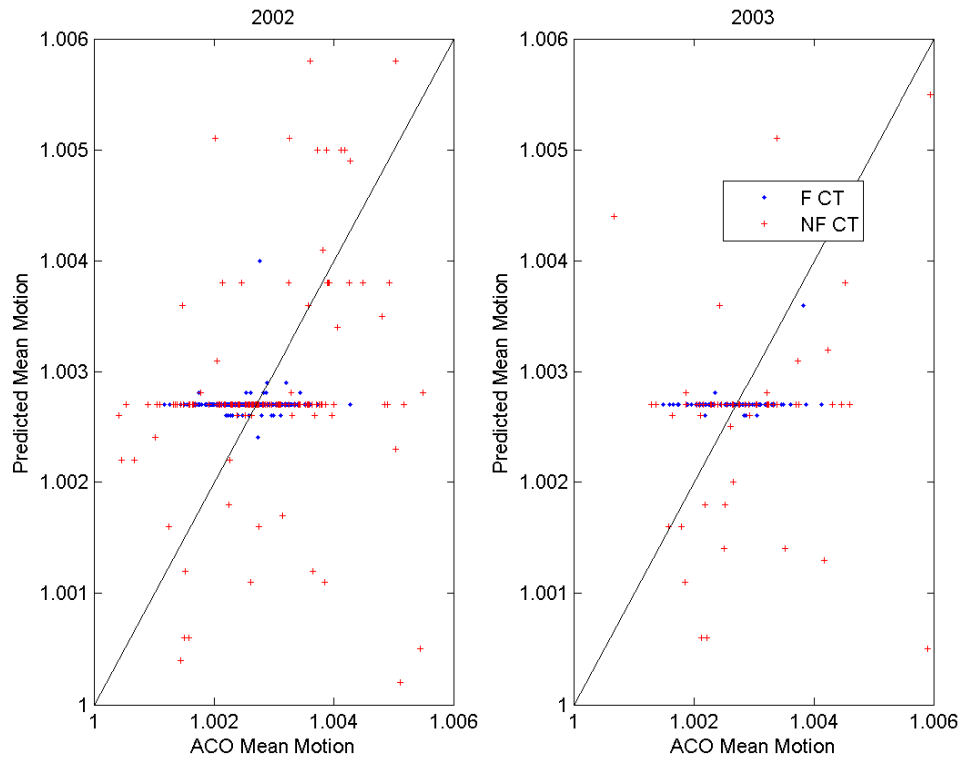


Figure 14. Comparison of inferred and known mean motion, concise range.

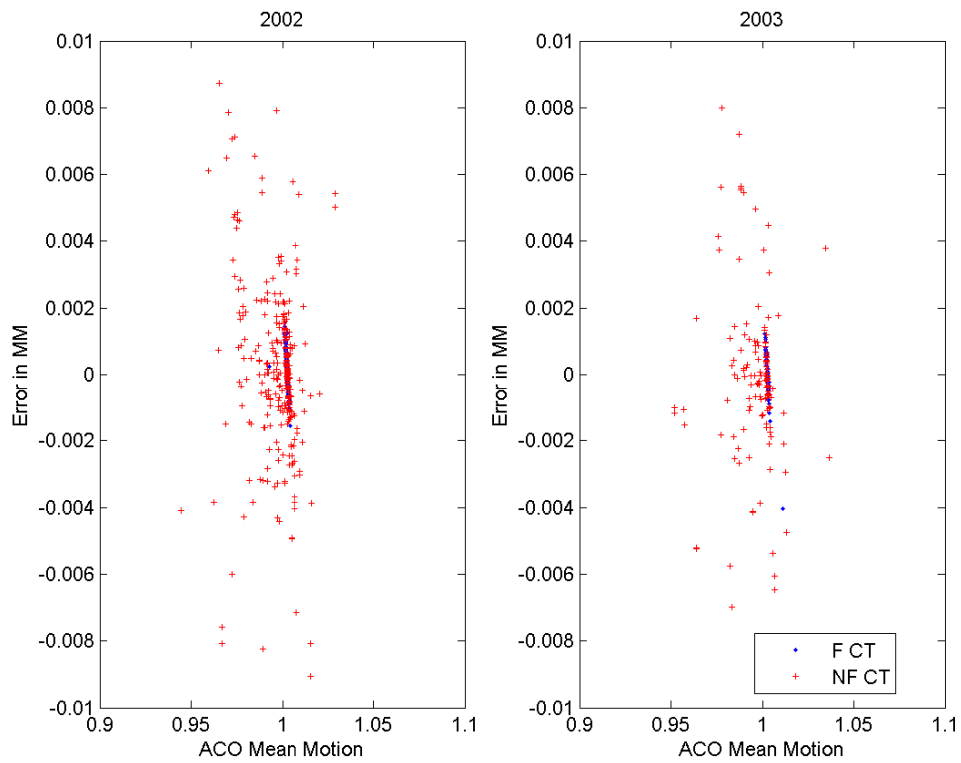


Figure 15. Mean motion error vs. ACO mean motion.

3.5.3.3 RAAN Determination

The calculation of RAAN is very difficult to determine accurately when the INC of the orbit is near 0° . Therefore, a breakdown of the data is shown for all objects as well as for objects with calculated INCs greater than 1° . The latter case is one thought to be more like debris. RMS error data for RAAN are shown in Table 3. As shown, the largest error occurs when objects with less than 1° INC are included. Once those are removed, the error is much smaller; an even smaller error is seen with the nonfunctional objects.

The data shown in Figure 16 are for the calculated vs. the predicted RAAN. Here it is shown clearly that the RAAN calculation for functional CTs, which nominally have 0° inclination, are erroneous. The nonfunctional CTs have good agreement with the predicted value of RAAN, showing that the calculation of RAAN is a valid calculation.

Table 3. RAAN Errors

Type of Error (reported in degrees)	All objects	All objects INCs > 1°	Nonfunctional objects	Nonfunctional objects INCs > 1°
RMS 2002	81	6	3	2
RMS 2003	80	4	25	2

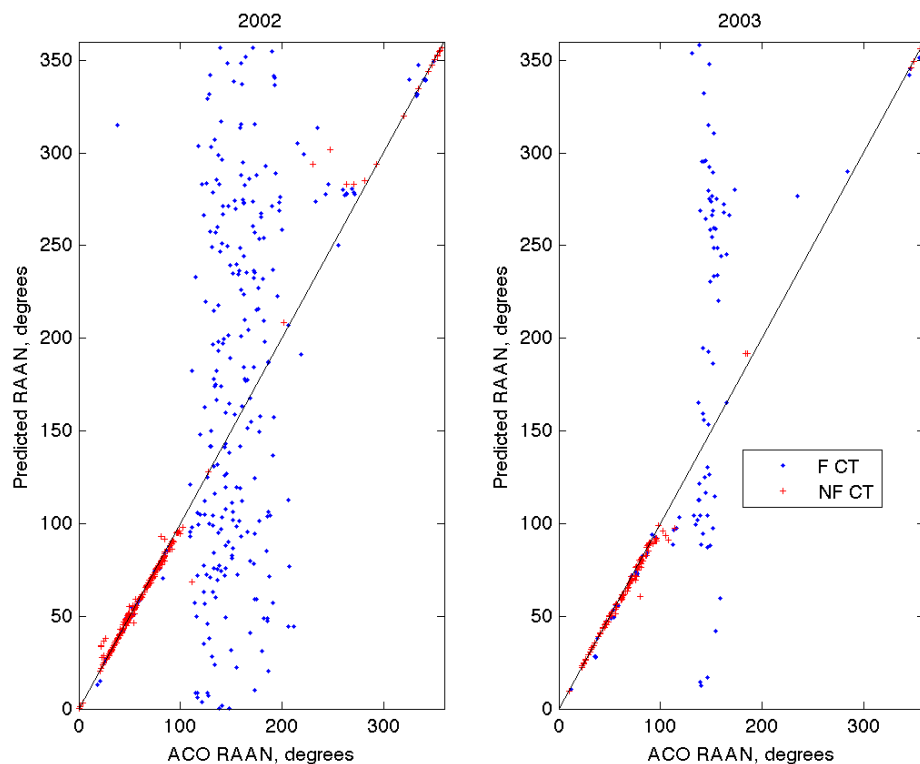


Figure 16. Comparison of inferred and known RAAN.

Figure 17 shows the error in the RAAN calculation compared to the ACO INC. Notice that objects with large errors are associated with very small INCs and are usually CT objects. Some interesting structure arises when the same plot is focused on the smaller errors, as shown in Figure 18. Two sets of arcs are seen in the nonfunctional CT data, and the trends are seen in both years of data. Errors in the RAAN calculation are small for these objects; however, the arcing shape seen in the figure is puzzling. Objects found along

this arc do not have anything in common in regards to date of collection, time of year, object number, or eccentricity. The only factor they have in common is that the lower the INC, the higher the error.

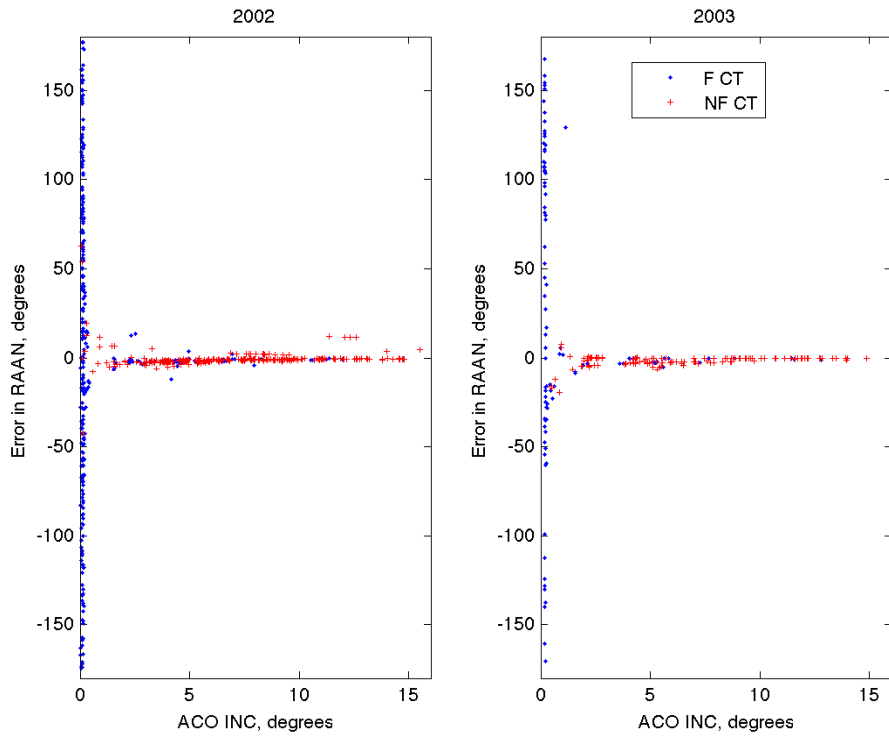


Figure 17. RAAN error as a function of INC.

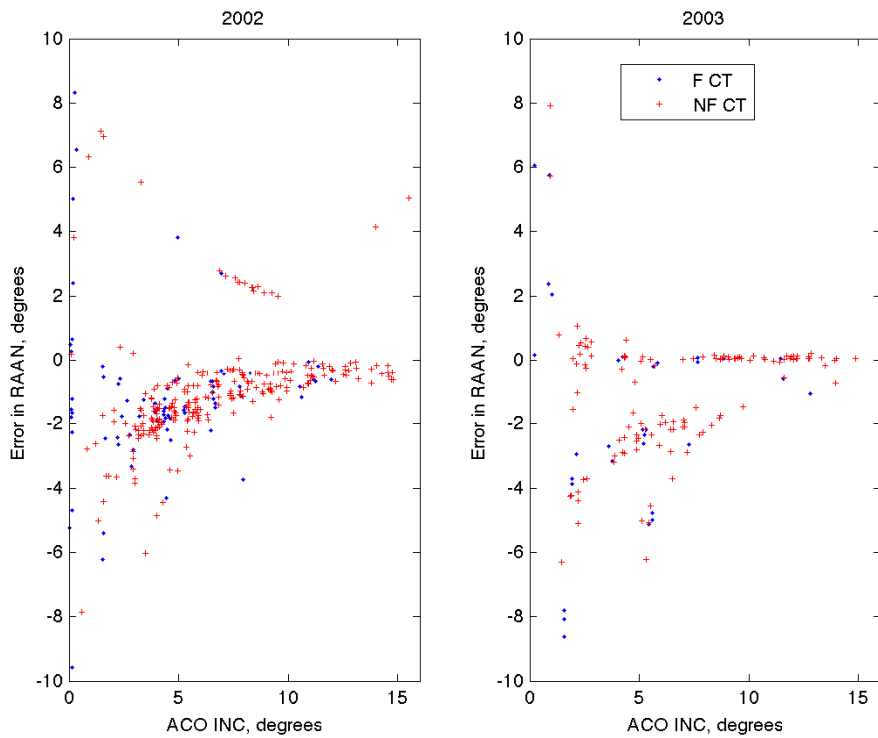


Figure 18. RAAN error (focus on smaller errors) as a function of INC.

3.6 Summary of Data Processing

Once the data are collected, the subsequent processing steps performed are:

- 1) Objects are identified as either CTs or UCTs.
- 2) Orbital elements (INC, range, RAAN, mean motion) for CTs are calculated from circular orbit fits, and biases or errors are determined to be applied to the UCT elements.
- 3) Sizes of detected objects are estimated, assuming an average albedo of 0.175 and a Lambertian phase function.
- 4) Probability of detection, defined as the likelihood of detection in a given orbit, is calculated based on the location of the telescope at a given time and date.

4.0 Results

4.1 Detection Rates

Thirty-five nights of data were reduced for CY 2002, starting with day of year (DOY) 009 and ending with DOY 315. For CY 2003, there were 16 nights of data, starting with DOY 032 and ending with DOY 272. In Table 4, the data collected are broken down into the different years. For each year, the percentage of CTs and UCTs observed, the average number of CTs and UCTs detected each night for all locations, and the average number of CTs and UCTs detected per night, when not on the GEO belt, are shown; ie, for those objects with INCs < 1°. The GEO belt is the nominal location of spacecraft that are being station-kept. Most of the objects in this regime are CTs; this is shown by the larger decrease in average number of objects collected for the CTs vs. those for the UCTs.

Table 4. Statistics on CY 2002 and CY 2003 Data Collection

Year	% CTs	% UCTS	Avg. # of CTs each night	Avg. # of UCTs each night	Avg. # of CTs – no belt	Avg. # of UCTs – no belt
2002	76%	24%	17	7	11	6
2003	67%	33%	15	8	11	8

4.2 Location of Field Centers and Detections

During a normal 2-week telescope run for the 2002–2003 data collection period, the strategy was to keep the RA unchanged while offsetting in declination by ± 1.2 degrees each night. In addition to this, the RA was chosen based on the location of the anti-solar point and closest proximity to that point possible without being in the shadow of the Earth. The data in Figure 19 show, using dots, a snapshot view of where objects are expected to be, given an RA and a DEC. These data are a snapshot of DOY 365 for 2003. The overall view of the plot will be similar regardless of the day used. The near-solid line of dots near 5° DEC is the location of the GEO belt as seen from CTIO. The red squares show the observing location of the telescope for each night in 2002; the blue squares show the locations for 2003. There is some overlap of field centers in 2002 and 2003 near 9° DEC. Note: The size of the square on the plot does not depict the size of the FOV for the telescope.

Once the field centers are determined, the data are run through a code that determines the probability of detecting an object in a specific orbit while at that FOV and specific given time. A probability chart, as shown in Figure 20, has different colors representing the probability of detection. The redder the color or the closer the probability is to 1, the greater the likelihood an object in that orbit was detected. Overlaid on the probability chart are the actual detections for the 2 years of data, for which the CTs are solid diamonds and the UCTs are open circles. With a larger number of nights collected, it would be possible to assess a population from these probability data. This is done in subsequent MODEST reports in which

more data were collected over the time frame reported. Once the probability chart was created, it was determined that FOV locations for future telescope runs could be predetermined by filling in areas of the probability chart. In future years, the goal is to have all areas covered with at least some color and to have all inclinations less than 15° have a probability of detection of at least 0.6. If this can be achieved, there is an excellent rationale for conducting a population assessment.

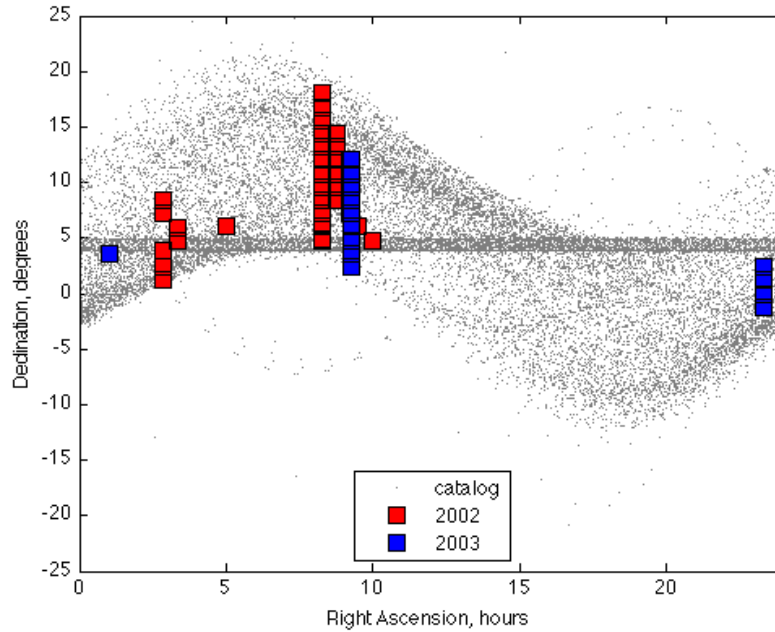


Figure 19. Location of field centers.

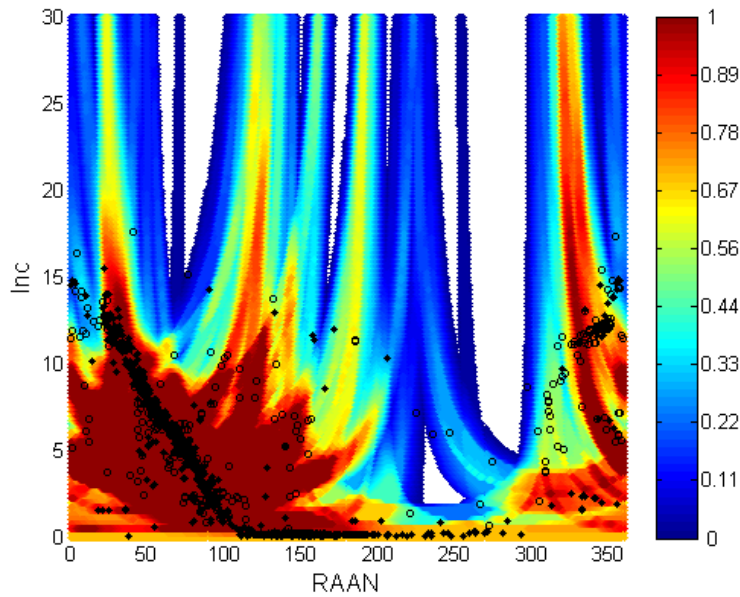


Figure 20. Probability of finding specific orbits based on field center locations.

4.3 Angular Momentum Vector

As previously discussed in Section 3.2, the orbits of GEO and near-GEO objects undergo precession under the influence of Earth's oblateness and the gravity of the sun and the moon. As this precession occurs, the ascending node also precesses such that, to the first order for "perfect" GEO objects, there is a one-to-one correspondence of INC to ascending node. A simple formula to show the relationship between INC i and RAAN is given by

$$\text{Cos}(i) \approx \frac{1 - [x \text{Cos}(RAAN)]^2}{1 + [x \text{Cos}(RAAN)]^2}$$

where

$$x = \frac{\text{Sin}(7.5^\circ)}{\text{Cos}(7.5^\circ)}.$$

This behavior can best be seen by the path of the angular momentum vector of the orbit, which traces an arc during this precession cycle centered about a line tilted 7.5° with respect to the north pole, as shown in Figure 21. An easy way to show the angular momentum vector for measured objects is to plot the orbital data in a polar graph with the ascending node as the polar angle and the INC as the radius.

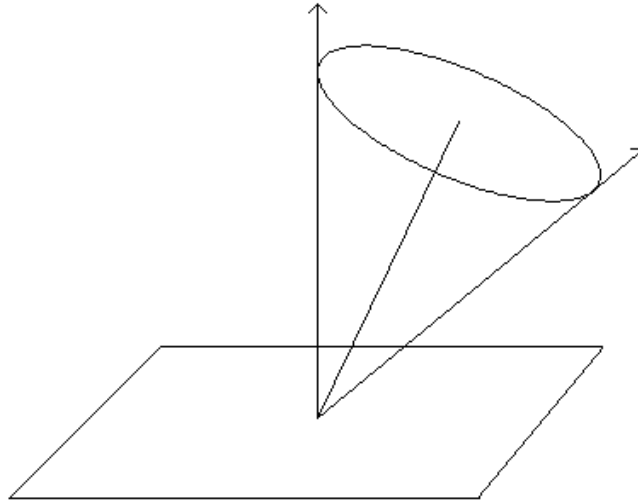


Figure 21. Angular momentum vector of an orbit.

In Cartesian terms,

$$\begin{aligned} x &= i \text{Cos}(RAAN) \\ y &= i \text{Sin}(RAAN). \end{aligned}$$

In these coordinates, the path traced out during the precession cycle is a loop. Objects found to reside on or near this idealized loop represent GEO or near-GEO objects at various stages in their orbital evolution or are objects perturbed by solar radiation pressure. Debris from energetic breakups may stray farther from this idealized path, depending on how strong the delta-velocity was they received at breakup.

The data collected in 2002 and 2003 are shown in Figure 22 and Figure 23, respectively. The plot has four subplots, which are termed polar plots due to the coordinate system shown. The upper left images show only the functional CTs as red, solid circles. One can see the data clustering around $X = 0$ and $Y = 0$. This was an expected result. The next two subplots show the nonfunctional CTs and the UCTs as blue, open circles and green, open circles, respectively. The data in these subplots show similar trends of the progression in orbital evolution or perturbations. The UCT data are more scattered and one theory being explored is that the solar radiation pressure is affecting these objects more than the nonfunctional CTs due to size and mass. Once all the data are plotted together (see the lower right plot), there appears to be an inner circle of data in all three data types; however, it is more apparent in the UCT data. The data shown for CY 2002 and CY 2003 have similar trends.

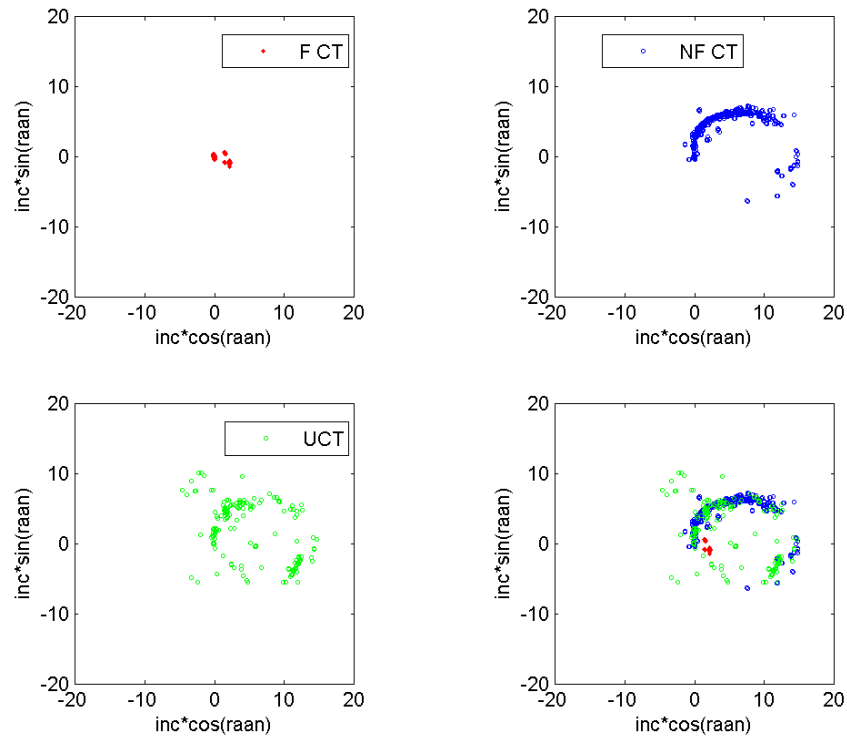


Figure 22. Polar coordinates for objects, CY 2002.

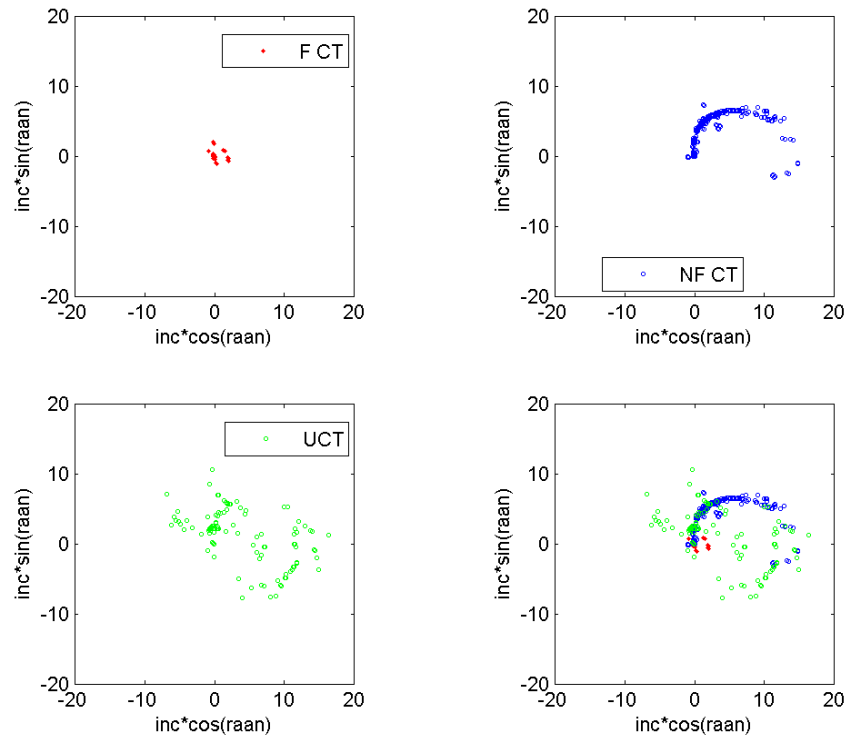


Figure 23. Polar coordinates for objects, CY 2003.

Figure 24 shows the probability of detection data converted into the polar data and overlaid with the 2002 and 2003 detections. This type of data is helpful to show where the next observing run should focus and to determine whether initial observations are in the right place.

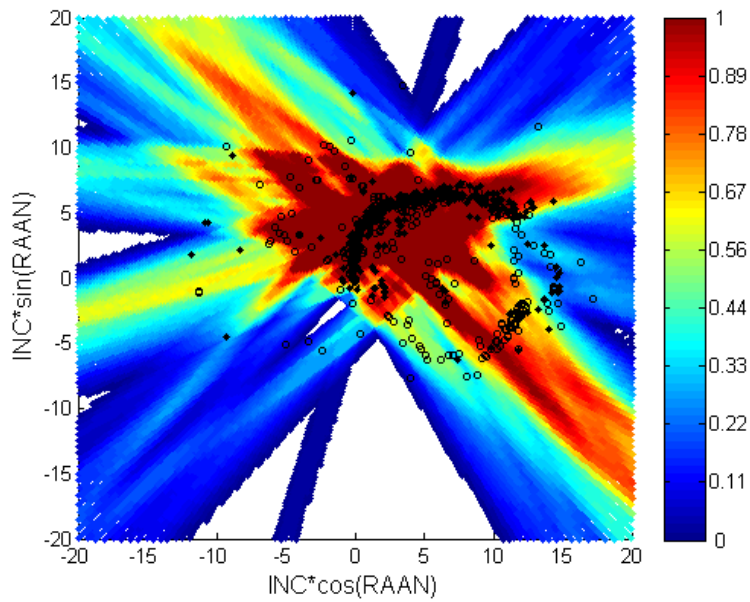


Figure 24. Polar coordinates with probability and detections overlaid.

4.4 No-sees

Data reduction includes predicting which known satellites from the U.S. SSN catalog will be seen in which observational frame. If a satellite is predicted to be present but evidence for its presence is not found, it is listed as a “no-see.” There are multiple potential reasons for an object’s non-detection, such as the object having too faint a visual magnitude or being outside of the rate box. In addition, the TLE used to predict an object’s location could be bad due to an old epoch date or station-keeping maneuvers. It is important to understand why an object is not seen, as it aids in understanding the debris environment and determining the limits of this method of analysis. Lack of detection of an object does not necessarily mean the object is not present; it can as easily indicate changes in the orbital elements, a breakup, or even changes in orientation. However, if a reason cannot be obtained for the no-see, it is labeled as a true no-see.

Over the 2-year period of 51 nights, 422 nonunique objects were considered no-sees for various reasons. Some of these may have been categorized as no-sees multiple times over the 2-year time frame. Of these 422 no-sees, 77% were due to rate box issues, 5% were due to bad TLE or 80,000s (80,000 objects are those that are in the catalog but have not been associated with a specific launch), 5% were due to bad/old epochs, and 12% were true no-sees.

Although an object may not be seen on a certain night, this does not rule out its detection on a different night. Of the 349 unique no-see CTs, 50 of these objects were detected and correlated on different nights. Of these 50 objects, 66% were rate issues, 32% were true no-sees, and 2% were 80,000s.

When the total number of detections over the 2-year time frame was compared to the total number of no-sees, a rate of 6% was deduced. This means that roughly 50 CTs could have been added to the 838 detected CTs. Assuming this rate is the same for UCTs, approximately 10 UCTs were missed. However, assuming the no-see rates for CTs and UCTs are the same could be presumptuous, since UCTs are complicated with complex shapes, photometric variations, and generally tend to be fainter than CTs. There does not appear to be a difference between the no-see rate for functional vs. nonfunctional CTs due to the fact that nonfunctional objects usually had older epochs while functional objects are maneuvered.

4.5 Mean Motion Distribution

The mean motion of most GEO objects is very close to 1 rev/day. The actual value usually seen for functional CTs in the TLEs shows a value closer to 1.0027 rev/day. The graph in Figure 25 compares mean motions for functional and nonfunctional CTs and UCTs. As expected, the large percentage of functional CTs is seen near a mean motion of 1 (97% of the objects collected). In addition, a large percentage of the nonfunctional CTs are also seen near 1 (43% of the objects collected). However, more nonfunctional CTs are spread throughout the various mean motions, similar to that of the UCTs. The UCTs have the highest percentage of objects near 1 rev/day at 17%; however, they are also seen at mean motions as small as 0.9 and as high as 1.08. Because of this variance, it is believed that the ACO calculation is inducing an error into the calculation of mean motion for these objects.

4.6 Inclination Distribution

As expected, the INC distribution for functional CTs aligns with 0° INC with 94% of the detected objects showing in that bin, as seen in Figure 26. Nonfunctional CTs are seen through all INC bins up to 15° to 16°, as expected due to the propagation of INC with orbital age; see Section 3.2 Search Strategy. The nonfunctional CTs have one peak near 5°. The UCTs have a similar spread in INC bins; however, two peaks appear to be located near 6° and 12° INC. Although the indication of two peaks could signal the location of a breakup, much more data would need to be collected prior to making a definitive statement. The data collected in the years following may prove useful in determining the reason for the two peaks.

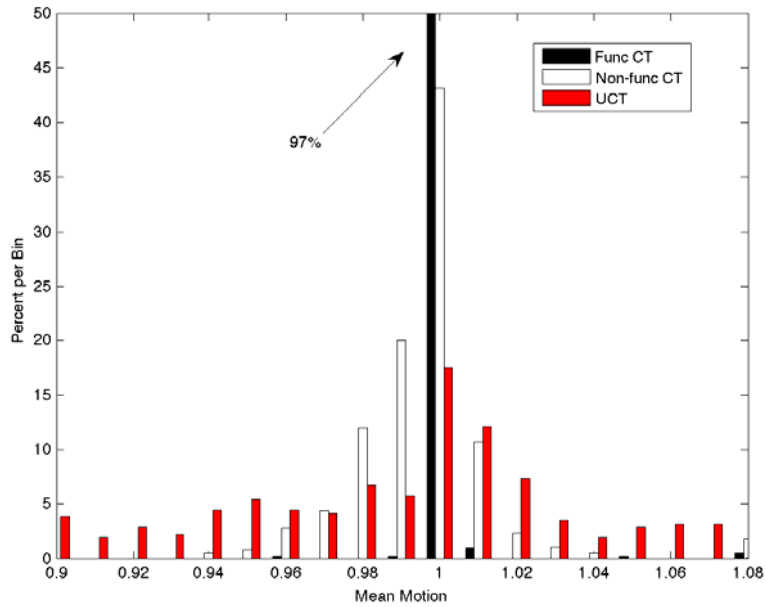


Figure 25. Mean motion distribution for CT and UCT objects.

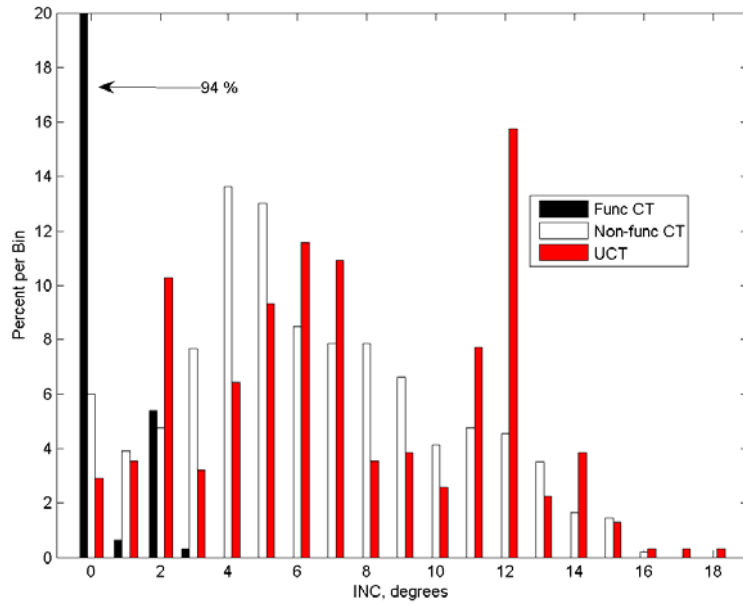


Figure 26. Distribution of INCs for CTs and UCTs.

4.7 RAAN Distribution

Distribution of RAAN in the functional CT, nonfunctional CT, and UCT populations is shown in Figure 27. As seen previously, the functional CT RAAN calculation concentrates on the region between 100° and 250° , whereas the nonfunctional CT and UCT populations are seen at all RAAN values. Two peaks of UCTs are also seen in these data, with the first located near 70° and the second located near 350° . This could be an indication of the same two breakups that were alluded to in the previous section. As with the INC distribution, one peak is located with the nonfunctional CTs near 80° .

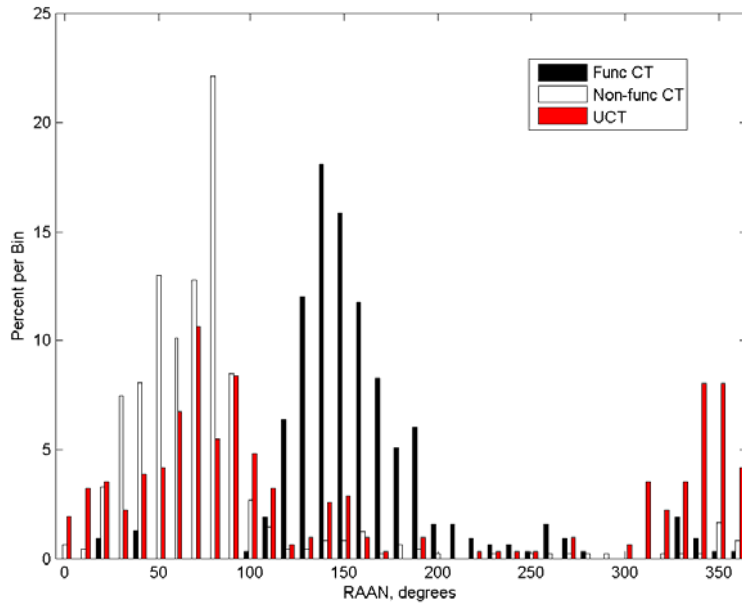


Figure 27. Distribution of RAAN for CTs and UCTs. The location of the data found is biased by the field center selection and the DOY.

4.8 Absolute Magnitude Distribution and Derived Diameters

As discussed in previous sections, the derived diameters stem from assuming an albedo of 0.175 and a diffuse Lambertian phase function.⁶ A mean distance of 36,000 km is also used. As a reminder, the absolute magnitude is a log calculation (unitless); the smaller the number, the brighter and, likely, larger the object. The distribution of absolute magnitudes is shown in Figure 28. Overlaid on the distribution are the diameters associated with a few of the bins. The peak in absolute magnitude for functional CTs is seen at 11, corresponding to a size of 4 m. The peak of the nonfunctional objects is seen near 12, which is a size of 2.5 m. The catalog is said to be complete down to 1 m at GEO; using the assumptions above, this corresponds to an absolute magnitude of 14.4. The peak of the UCTs is an artificial one due to the detection capabilities of the telescope. It is believed the UCT population will continue on the same slope throughout the smaller magnitudes. As described in this report, the smallest detected object to be seen with MODEST, using the albedo and phase function assumptions, is 10 cm.⁶

4.9 RAAN vs. INC Distribution

INC and RAAN distributions for the detected objects are illustrated in Figure 29. The top figure shows the data collected in 2002, and the bottom figure shows the data collected in 2003. These data present a collection of UCTs near 350° RAAN and 12° INC. This is believed to be the location of the Titan breakup. Similar clustering is observed near 70° RAAN and 5° INC as well as near 90° RAAN and 3° INC; however, no known breakups have occurred in those areas. The clusters may indicate locations of unknown breakups but more data need to be collected to confirm these findings. The data in these plots show the expected climb toward 15° INC for the UCTs and nonfunctional CTs as well as for the functional CTs at various RAANs with 0° INC.

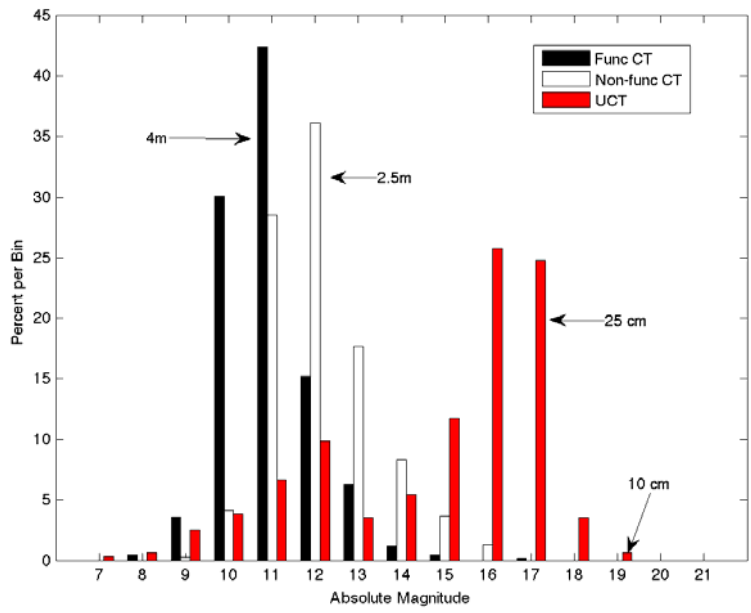


Figure 28. Absolute magnitude and derived size distribution, assuming an albedo of 0.175 and a diffuse Lambertian phase function.

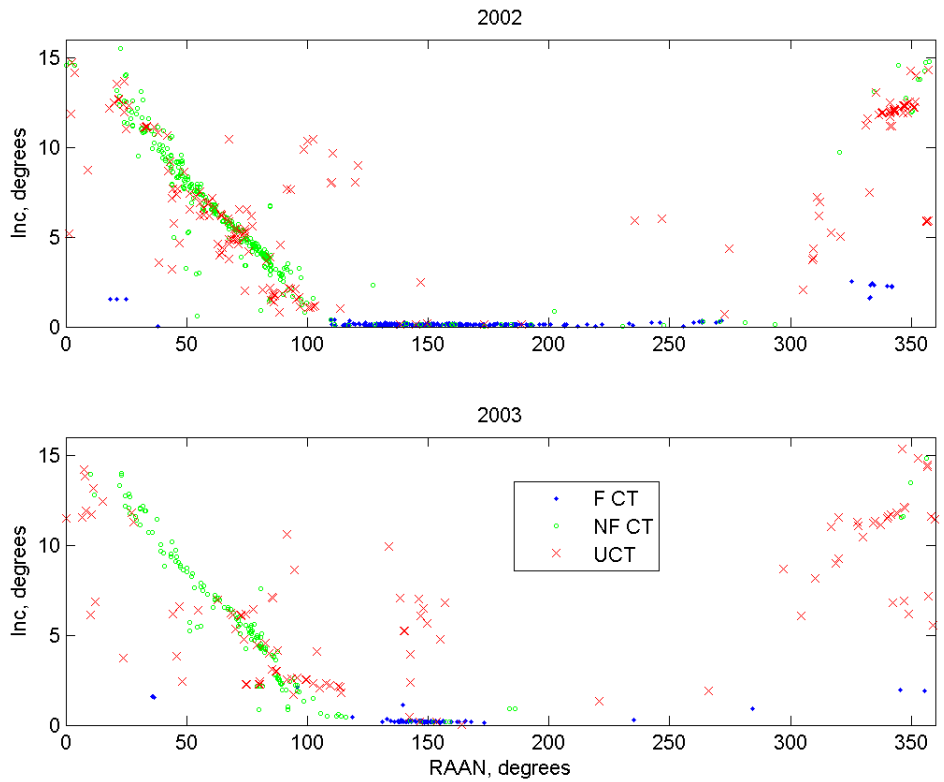


Figure 29. RAAN vs. INC for CT and UCT objects.

5.0 Conclusions

This JSC report provides details of observational and data-reduction processes for the entire MODEST dataset acquired in CY 2002 and CY 2003. Specifically, this report describes the collection and analysis of 35 nights of data collected in CY 2002 and of 16 nights of data collected in CY 2003.

For both years, averages of 22 objects were detected each night. On average in CY 2002, 76% of the detections were CTs and 24% were UCTs, whereas in CY 2003 the percentages were 67% and 33% for CTs and UCTs, respectively. The variation in percentages between the years may be due to observing in different locations with respect to the GEO belt.

Errors associated with the derived quantities of range, INC, and RAAN were derived by comparing values calculated using an ACO and those known values seen in the TLE. The average INC RMS error is 0.1° for functional CTs and 0.3° for nonfunctional CTs. Due to the fact that RAAN is ill-defined at values of 0° INC, the RMS error for RAAN is calculated only for objects with an INC greater than 1° . The average RAAN RMS error is 20° for functional objects and 11° for nonfunctional objects in CY 2002, and 57° for functional objects and 16° for nonfunctional objects in CY 2003. For CY 2002, the mean motion error is 0.0005 rev/day for functional and 0.0070 rev/day for nonfunctional objects, and 0.0071 rev/day and 0.0091 rev/day for functional CTs and nonfunctional CTs, respectively. This error analysis of CT values for INC, RAAN, and mean motion lends credibility to the determination of the UCT orbital element distributions.

The distribution of objects found UCTs clustering in three locations, with only one cluster corresponding to the breakup of Titan. More data are needed to confirm whether the other two clusters could be from unknown breakups.

The absolute magnitude distribution showed a peak for the functional CTs at 11th magnitude. An absolute magnitude of 11.5 corresponds to objects having average diameters of 4 m, assuming an albedo of 0.175 and a diffuse Lambertian phase function. This result generally agrees with the known sizes of intact satellites. The absolute magnitude distribution for the UCTs is broad, but starts to roll off near a diameter of 29 cm or 17.5 magnitude. The roll off in the distribution reflects the detection capability of MODEST and does not reflect the true nature of the population. The true population is believed to continue at the same slope through fainter magnitudes.

6.0 References

- ¹Johnson, N.L., et al. "History of On-Orbit Satellite Fragmentations." *JSC-29517*, Houston, TX, 2001.
- ²Pensa, A. F., et al. "Debris in Geosynchronous Orbit." *SPACE FORUM*, Vol. 1, pp. 23 – 27, 1996.
- ³Talent, D. L. et al. "A Search for Debris in GEO." *Proceedings of the Second European Conference on Space Debris*, Darmstadt, Germany, 1997.
- ⁴Friesen, L. et al. "Results in Orbital Evolution of Objects in the Geosynchronous Region." AIAA 90-1362, *AIAA/NASA/DOD Orbital Debris Conference: Technical Issues and Future Directions*, Baltimore, MD, 1990.

⁵Vaughan, S. H. and Mullikin, T. L. “Long Term Behavior of Inactive Satellites and Debris Near Geosynchronous Orbits.” AIAA 95-200, *AAS/AIAA Spaceflight Mechanics Meeting*, Albuquerque, NM, 1995.

⁶Mulrooney, M.K., Matney, M.J., and Barker, E.S. “A New Bond Albedo for Performing Orbital Debris Brightness to Size Transformations.” *International Astronautical Congress*, Glasgow, Scotland, 2008.

⁷Press, W.H., Teukolsky, S.A, Vetterling, W.T., and Flannery, B.P. *Numerical Recipes in Fortran 90*. Cambridge University Press. Volume 2. January 1996.

⁸Hoots, F.R. and Roehrich, R.L. “Spacetrack Report #3: Models for Propagation of the NORAD Element Sets.” U.S. Air Force Aerospace Defense Command, Colorado Springs, CO.

Appendix A: Fields File Example

(This is a representative sample of the file)

DEC	RA	Time (sec)	Frame
4.842	124.306	10368.1	19
4.842	124.306	10406.0	20
4.842	124.306	10443.9	21
4.842	124.306	10481.8	22
4.842	124.306	10519.7	23
4.842	124.306	10557.6	24
4.842	124.306	10595.5	25
4.842	124.306	10633.4	26
4.842	124.306	10671.3	27
4.842	124.306	10709.2	28
4.842	124.306	10747.1	29
4.842	124.306	10785.1	30
4.842	124.306	10822.9	31
4.842	124.306	10860.8	32
4.842	124.306	10898.7	33
4.842	124.306	10936.6	34
4.842	124.306	10974.6	35
4.842	124.306	11012.5	36
4.842	124.306	11050.4	37
4.842	124.306	11088.3	38
4.842	124.306	11126.2	39
4.842	124.306	11164.1	40
4.842	124.306	11202.0	41
4.842	124.306	11239.9	42
4.842	124.306	11277.8	43
4.842	124.306	11315.7	44
4.842	124.306	11353.6	45
4.842	124.306	11391.5	46
4.842	124.306	11429.4	47
4.842	124.306	11467.3	48
4.842	124.306	11505.2	49

Appendix B: Output File Example

The columns are frame number, RA, DEC, epoch, magnitude, date, and time. Two objects are shown, both with nine detections. This output is what NASA receives from the telescope.

```
2002009.0001 9
29 123.6621 4.8225 2000.0 11.3 2002-01-09 2.98532
30 123.8204 4.8225 2000.0 11.3 2002-01-09 2.99585
31 123.9782 4.8225 2000.0 11.3 2002-01-09 3.00637
32 124.1370 4.8225 2000.0 11.3 2002-01-09 3.01690
33 124.2953 4.8232 2000.0 11.3 2002-01-09 3.02743
34 124.4537 4.8243 2000.0 11.3 2002-01-09 3.03795
35 124.6126 4.8244 2000.0 11.3 2002-01-09 3.04849
36 124.7703 4.8244 2000.0 11.3 2002-01-09 3.05902
37 124.9286 4.8244 2000.0 11.3 2002-01-09 3.06955
2002009.0002 9
50 123.6602 4.8534 2000.0 11.2 2002-01-09 3.20642
51 123.8191 4.8534 2000.0 11.2 2002-01-09 3.21695
52 123.9768 4.8534 2000.0 11.2 2002-01-09 3.22747
53 124.1358 4.8534 2000.0 11.2 2002-01-09 3.23800
54 124.2943 4.8543 2000.0 11.0 2002-01-09 3.24853
55 124.4524 4.8534 2000.0 11.2 2002-01-09 3.25907
56 124.6103 4.8539 2000.0 11.2 2002-01-09 3.26959
57 124.7690 4.8553 2000.0 11.2 2002-01-09 3.28012
58 124.9276 4.8553 2000.0 11.2 2002-01-09 3.29065
```

Appendix C Correlation Output

These data are from the correlation file for the two objects listed in Appendix B. The computer program correlated one object, and the other object was correlated by hand.

	newRAoffset	newDECoffset	newsquare	Match	Mag	UT	OMM	OINC	ORAAN	AM PRANGE	PECC	PINC	PMM	PRAAN		
11	1 to 21765	-0.009645	-0.007828	0.012422	CORRELATES	11.3	2.98532	1.00264220	0.0947	117.1440	11.0	37995	0.0000960	0.00	1.0027	8.82
12	1 to 21765	-0.010087	-0.007838	0.012774	CORRELATES	11.3	2.99585	1.00264220	0.0947	117.1440	11.0	37995	0.0000960	0.00	1.0027	8.82
13	1 to 21765	-0.010196	-0.007849	0.012867	CORRELATES	11.3	3.00637	1.00264220	0.0947	117.1440	11.0	37995	0.0000960	0.00	1.0027	8.82
14	1 to 21765	-0.009721	-0.007858	0.012500	CORRELATES	11.3	3.01690	1.00264220	0.0947	117.1440	11.0	37995	0.0000960	0.00	1.0027	8.82
15	1 to 21765	-0.009746	-0.007168	0.012098	CORRELATES	11.3	3.02743	1.00264220	0.0947	117.1440	11.0	37995	0.0000960	0.00	1.0027	8.82
16	1 to 21765	-0.009672	-0.006077	0.011423	CORRELATES	11.3	3.03795	1.00264220	0.0947	117.1440	11.0	37995	0.0000960	0.00	1.0027	8.82
17	1 to 21765	-0.009515	-0.005986	0.011241	CORRELATES	11.3	3.04849	1.00264220	0.0947	117.1440	11.0	37995	0.0000960	0.00	1.0027	8.82
18	1 to 21765	-0.010142	-0.005996	0.011782	CORRELATES	11.3	3.05902	1.00264220	0.0947	117.1440	11.0	37995	0.0000960	0.00	1.0027	8.82
19	1 to 21765	-0.010167	-0.006004	0.011807	CORRELATES	11.3	3.06955	1.00264220	0.0947	117.1440	11.0	37995	0.0000960	0.00	1.0027	8.82
32	2 to 23413	0.050185	0.033890	0.060556		11.2	3.20642	1.00277416	0.0699	111.6942	10.9	37798	0.0001629	0.01	1.0026	182.58
33	2 to 23413	0.050687	0.033860	0.060956		11.2	3.21695	1.00277416	0.0699	111.6942	10.9	37798	0.0001629	0.01	1.0026	182.58
34	2 to 23413	0.049991	0.033830	0.060362		11.2	3.22747	1.00277416	0.0699	111.6942	10.9	37798	0.0001629	0.01	1.0026	182.58
35	2 to 23413	0.050594	0.033800	0.060846		11.2	3.23800	1.00277416	0.0699	111.6942	10.9	37798	0.0001629	0.01	1.0026	182.58
36	2 to 23413	0.050698	0.034669	0.061418		11.0	3.24853	1.00277416	0.0699	111.6942	10.9	37798	0.0001629	0.01	1.0026	182.58
37	2 to 23413	0.050401	0.033739	0.060651		11.2	3.25907	1.00277416	0.0699	111.6942	10.9	37798	0.0001629	0.01	1.0026	182.58
38	2 to 23413	0.049905	0.034209	0.060504		11.2	3.26959	1.00277416	0.0699	111.6942	10.9	37798	0.0001629	0.01	1.0026	182.58
39	2 to 23413	0.050209	0.035580	0.061538		11.2	3.28012	1.00277416	0.0699	111.6942	10.9	37798	0.0001629	0.01	1.0026	182.58
40	2 to 23413	0.050412	0.035549	0.061686		11.2	3.29065	1.00277416	0.0699	111.6942	10.9	37798	0.0001629	0.01	1.0026	182.58
